FINAL REPORT FOR:

DETECTION AND CONTROL OF INSTABILITIES AND BLOWOFF FOR LOW EMISSIONS COMBUSTORS

NASA Cooperative Agreement NNX07AC92A
Final Report

SUBMITTED BY: GEORGIA INSTITUTE OF TECHNOLOGY

SCHOOL OF AEROSPACE ENGINEERING

POINT OF CONTACT: PROFESSOR JERRY SEITZMAN

SCHOOL OF AEROSPACE ENGINEERING

ATLANTA, GA. 30332 – 0150

(404) 894-0013

(404) 894 – 2760, FAX

jerry.seitzman@aerospace.gatech.edu

I.   EXECUTIVE SUMMARY

One of the major concerns for future supersonic aircraft is low pollutant emissions over the complete operational flight regime. Most methods currently envisioned to limit emissions involve tight restrictions on local fuel-air distribution in order to reduce peak combustion temperatures. However, lean low-emissions combustors are prone to various instability problems, including lean blowout (LBO or static instability), and dangerously high pressure fluctuations caused by coupling of the heat release and the combustor acoustics (dynamic instability). Thus, operation of future clean engines requires a tradeoff between low emissions operation, and engine reliability and operability. The optimal approach to manage this tradeoff over the wide range of conditions that an aeroengine experiences during a complete operational flight cycle and over an engine lifetime is active control. This report describes research on the fundamental knowledge and technology development required to develop comprehensive stability control systems in a turbine engine combustor. This research program directly addresses one of NASA's strategic goals (Goal 3), as laid out in the 2006 NASA Strategic Plan. Specifically, it advances knowledge in the fundamental disciplines of aeronautics and aids in the development of technologies for improved aircraft safety and higher capacity airspace systems.

This program covered the development and demonstration of the sensor and control approaches necessary to enable active control of fuel-air spatial and temporal distribution in a turbine engine combustor in order to operate with minimal NOx emissions, while ensuring system stability and reliability. Our approach was to use nonintrusive sensors, e.g., acoustic and optical, which are based mostly on proven hardware and able to operate reliably in the combustor section of a modern gas turbine engine, and which can, with *proper interpretation*, be employed to determine **proximity to - or for feedback control of - lean blowout (LBO) and combustion instability**. Specifically, we examined elements of a hierarchical stability control system that incorporates three lower level control systems that would share the same fuel actuators. An **Active Static Stability Control (ASSC)** provides static stability through relatively low bandwidth spatial fuel redistribution. **Active Instability Margin Management** (**AIMM**) control is intended to slowly adjust the combustor conditions (fuel distribution) in order to prevent conditions conducive to dynamic instability; while **Active Instability Control (AIC)** suppresses the pressure fluctuations through medium bandwidth fuel modulation.

Some of the major accomplishments and findings of this effort are:
1. Optical approaches employing rugged, fiberoptically coupled devices are a viable approach for robust sensing and control of combustion zone fuel-air ratio and LBO proximity.
2. A dynamic instability margin estimator can provide improved time response for an AIMM system, while maintaining sufficient accuracy in the margin estimate.
3. With regard to AIC systems, it is crucial to include time-delays of internal and external (controller) feedback loops for self-excited combustors to capture controller performance trends. New analysis tools were developed for combustor control design with a focus on multimode stability and placement of non-minimum phase zeroes and poles, and the results provide insight into tradeoffs in performance, robustness and uncontrolled system stability.
4. A single, robust LBO margin sensing approach, based on detection of extinction/ignition precursors, was demonstrated that can be employed in a wide range of combustion system, including low NOx Jet-A fueled systems, even in the presence of combustion dynamics. New stochastic analysis methods were developed to design and predict the performance of both optimal (slow response) and fast (transient operation) LBO controllers potential for improved engine performance without loss of reliability/operability.

II.   OBJECTIVES, RELEVANCE AND APPROACH

One of the major concerns for future supersonic aircraft is low pollutant emissions over the complete operational flight regime.[1] While various approaches have been proposed for lowering NO_x emissions from aircraft engine combustors, most methods currently envisioned involve tight restrictions on local fuel-air distribution. In general, low-emissions engines envisioned for supersonic aircraft depend on reduced combustor liner cooling air[2] and rapid mixing between fuel and combustion air. For example, lean prevaporized-premixed (LPP) combustors rely on quick atomization and fuel-air mixing to achieve a lean premixed combustion zone. Similarly, various advanced combustor designs rely on rapid mixing injectors, e.g., using multiple swirlers, to create a lean, partially premixed combustion system. Another approach, lean direct injection (LDI), relies on distributed injectors to achieve efficient fuel-air mixing and lean combustion in a compact region. These approaches are prevalent because lean combustion, **which produces low peak temperatures**, produces low pollutant emissions, especially NOx.[3] Another key to reducing NOx emissions is minimizing residence time of combustion products at high temperatures.

II.A   Objectives

However, highly lean combustors are prone to various instability problems. For example, transient flame holding issues include inability to stabilize the flame in the combustor,[4] denoted lean **blowout** (LBO), and flashback and/or autoignition into the prevaporizer section (in LPP systems). One way to improve flame stability is to tailor the fuel-air distribution so as to provide a more stable (locally richer, high heat release) flame holding region. Of course, this leads to higher emissions. Of perhaps more concern under lean operation is the potential for dangerously high pressure fluctuations caused by coupling of the heat release and the combustor acoustics (**combustion dynamics/instability**). Thus, operation of future clean engines requires a tradeoff between low emissions operation, and engine reliability and operability.

In addition, low emissions combustors for supersonic aircraft must be designed for complete operational cycle impact. Producing low NOx emissions for supersonic aircraft requires a careful tradeoff between takeoff, climb and supersonic cruise conditions.[1] In order to maintain the balance between low emissions and safe operation across the wide range of power requirements and flight conditions, designers of future engine combustors will require technologies that allow them to **control fuel-air distribution** (temporally and spatially) in a way that will produce **lean but stable** combustion with **minimal residence time**. This requires the development of combustion systems that have the ability to control fuel placement and sensors to monitor fuel-air mixing/distribution and proximity of the combustor to unsafe operation.

II.B   Relevance

This research program directly addressed one of NASA's strategic goals (Goal 3) laid out in the 2006 NASA Strategic Plan. Specifically, it addressed Sub-goal 3E and Outcome 3E.1, in that it advanced knowledge in the fundamental disciplines of aeronautics and should aid in the development of technologies for improved aircraft safety and higher capacity airspace systems. The propulsions systems needed to power environmentally friendly, supersonic aircraft will have to operate under conditions that do not allow designers the freedom to incorporate wide combustor stability margins using passive approaches. Therefore, active combustion control technologies will be needed to ensure that supersonic aircraft propulsion systems can operate stably, and with high efficiency and low emissions over the wide range of flight conditions that

will occur.

II.C Vision and Approach

This research program covered the development and demonstration of sensor and control approaches necessary to enable active control of fuel-air spatial and temporal distribution in a turbine engine combustor in order to operate with minimal NOx emissions, while ensuring system stability and reliability. Our approach was characterized by the axiom "**simple sensing, smart processing**," using nonintrusive, e.g., acoustic and optical sensors that are based mostly on proven hardware, which are able to operate reliably in the combustor section of a modern gas turbine engine, and which can, with *proper interpretation*, be employed to determine **proximity to - or for feedback control of - lean blowout and combustion instability**. Thus our emphasis has been to improve the understanding of the relationship between the sensor outputs and the combustor status, including stability proximity, dynamic instability properties (frequency/phase) and fuel-air distribution in the heat release region.

Specifically, we are examining the elements of a hierarchical stability control system that incorporates three lower level control systems that share the same fuel actuators. An **Active Static Stability Control (ASSC)** provides static stability through relatively low bandwidth spatial fuel redistribution. Two systems ensure dynamic stability: an **Active Instability Margin Management** (**AIMM**) control, that slowly adjusts the combustor conditions (fuel distribution) in order to prevent conditions conducive to dynamic instability; and an **Active Instability Control (AIC)**, that suppresses the pressure fluctuations through medium bandwidth fuel modulation should the combustor be forced into an unstable operating condition by rapid changes beyond the capability of the AIMM controller.

Thus the work was divided into four tasks, with the third and fourth tasks representing the main focus of the program.

1. Fuel-Air Ratio Sensing
2. Active Instability Margin Management
3. Active Instability Control
4. Active Static Stability Control

III. RESEARCH RESULTS AND ACCOMPLISHMENTS

The accomplishments for the each of the tasks during the program are described below.

III.A Fuel-Air Ratio Sensing

The goal of this task was to provide an extra input to a fuel-control system that provides an indication of the local fuel-air ratio in the heat-release region. One of the driving mechanisms for both dynamic and static instability is perturbation of the fuel-air ratio; small decreases in fuel-air ratio for even short durations can lead to instability. We used the natural chemiluminescence produced by the chemical reactions to determine the reaction zone, fuel-air ratio. This approach requires relatively simple optical sensors, which can be remotely located from the combustor by using optical fibers to collect the chemiluminescence.[5]

In a previous NASA program (NCC3-982), we obtained Jet-A chemiluminescence data for emissions from CH*, OH* and C_2* in a laminar, lean prevaporized and premixed (LPP) Jet-A/air

flame. Two ratios obtained from these three species (after correction for broadband background emission) are shown in Figure 1. As can be seen, both the CH*/OH* and C$_2$*/OH* ratios monotonically increase with fuel-air ratio. The specific objective of the current effort was to demonstrate the approach in combustor operating at elevated pressure using liquid (Jet-A) fuel.

Our first step toward this was to determine if the characterization experiments in the prevaporized burner were relevant to a liquid-fueled combustor. Figure 2 shows a comparison of the data obtained in the laminar LPP burner, where the local fuel-air is well known, with data obtained in a rapid mixing, swirled spray burner.[5] The excellent agreement indicates the validity of the approach.
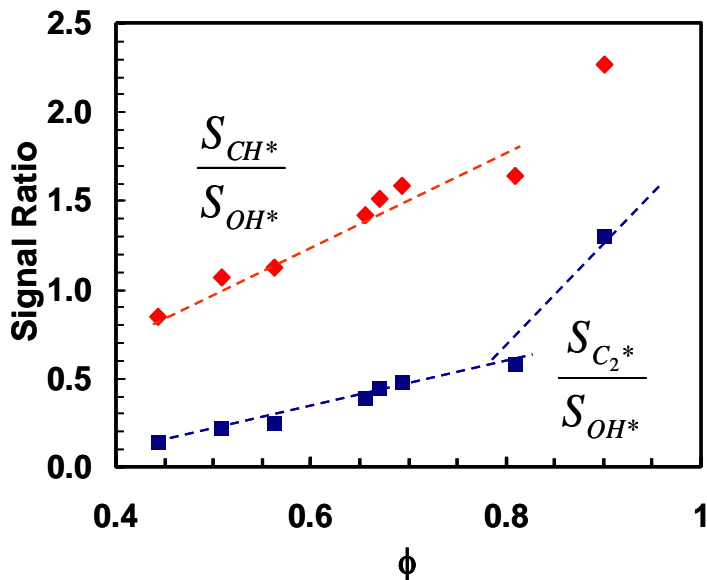
Figure 1. Experimental measurements of two chemiluminescence ratios from a prevaporized, laminar Jet-A flame.
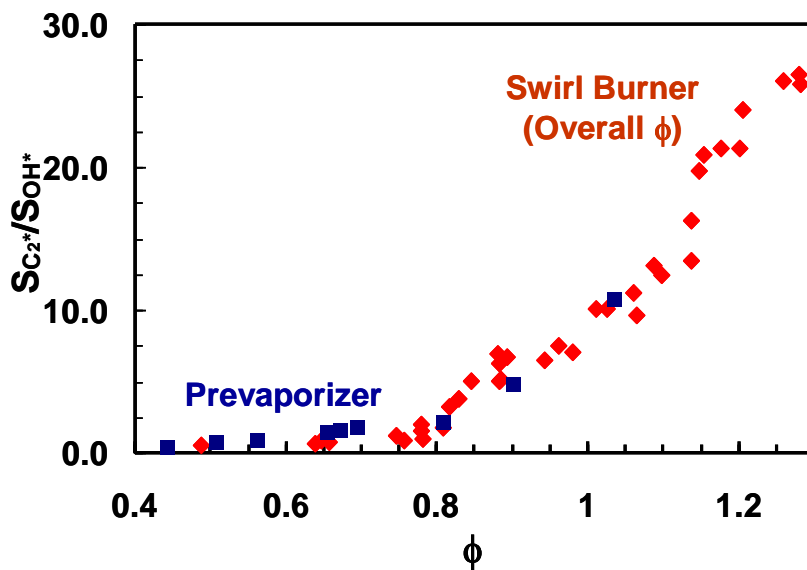
Figure 2. Comparison of chemiluminescence ratio from a prevaporized, laminar Jet-A flame and the ratio in a Jet-A fueled, rapidly mixing swirl combustor.

We later examined acquired data in a Lean Direct Injection (LDI) combustor at elevated pressure. The combustor was based on a NASA design (see Section III.D.1). Results from simultaneous sensing using a commercial pair of solid-state PMT detectors fiberoptically coupled to the combustor rig are shown in Figure 3. The results agree with previous simulation results showing the monotonic increase in the ratio of the chemiluminescence from CH* to that from OH* as the fuel-air ratio of the combustion zone is increased (e.g., Figure 1). In addition, the predicted increase[6] in the ratio as pressure is increased is also observed in the data.

Overall, we concluded that chemiluminescence based sensing of burning zone fuel-air ratio in lean-burn Jet-A fueled combustor is a viable approach for providing feedback to an engine control system.
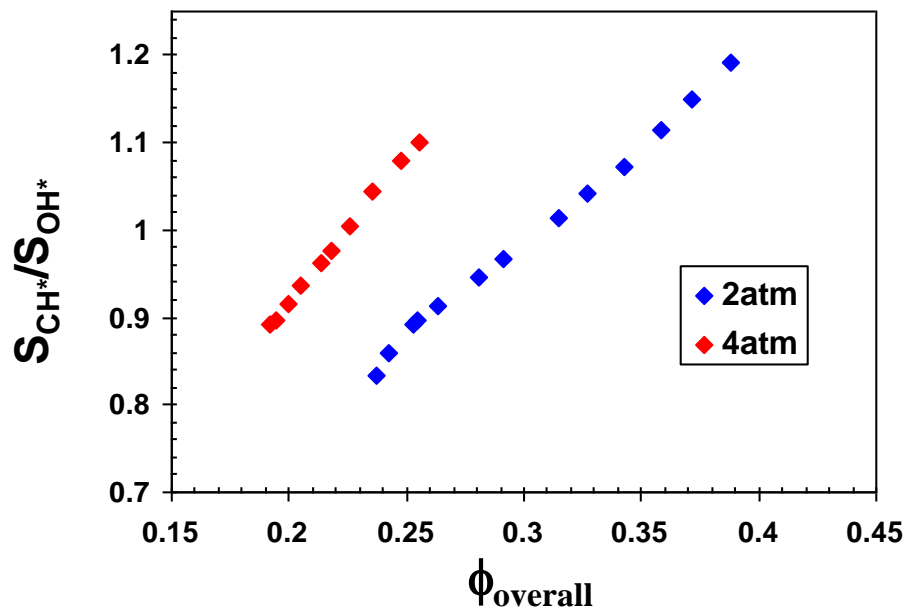

Figure 3. Comparison of chemiluminescence ratio from a prevaporized, laminar Jet-A flame and the ratio in a Jet-A fueled, rapidly mixing swirl combustor.

III.B Active Instability Margin Management

In this task, we examined methods to improve the estimate of instability margin, to improve time response for estimates, to understand sources of uncertainty in this estimate, and to quantify the tradeoffs associated with measurement accuracy and time response.

Work began with generating an experimental dataset for consideration.[7] A swirl stabilized combustor, with lengths of 300 and 600 mm, was used under atmospheric conditions burning natural gas. This combustor was operated over a range of conditions where it was nominally "stable" and where instability conditions were approached. Data was collected at 5 kHz using a Brüel and Kjaer microphone and associated conditioning amplifier near the exit of the combustor.

A fast Fourier transform was used to extract the dominant frequency, which corresponds to the quarter wave mode as seen in Figure 4 and Figure 5. This frequency was then used as the

center frequency of a 1st order bandpass filter with a width of 20 Hz in order to isolate the contribution of the dominant frequency to the pressure oscillations from the background noise and other tones present. The filtered data was used to calculate the autocorrelation function *C* (Eq. A).
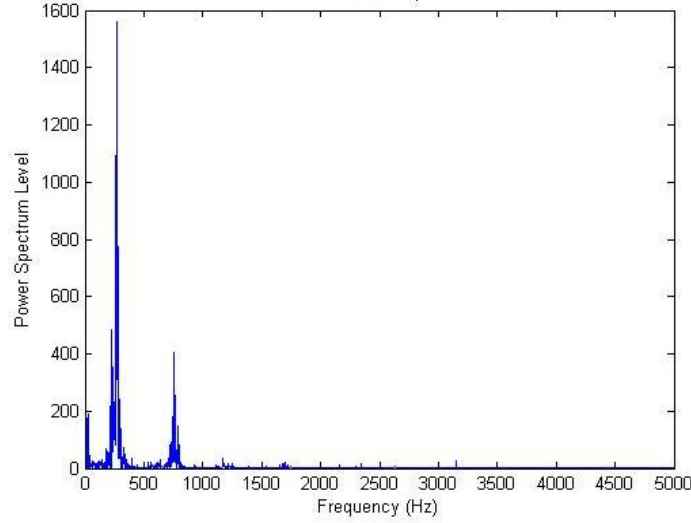

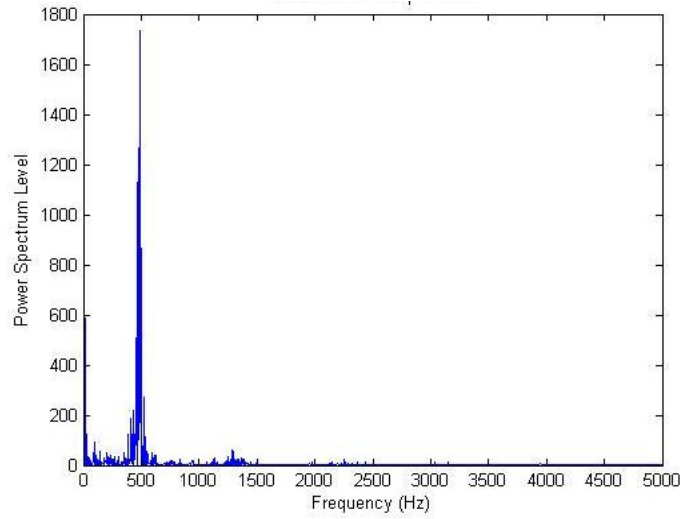Figure 4. PSD of 600 mm combustor for equivalence ratio of 0.42.

Figure 5. PSD of 300 mm combustor for equivalence ratio of 0.42.

$$C_i(\tau) = \frac{\int_0^T p_i(t)p_i(t+\tau)dt}{\int_0^T p_i^2(t)dt} \tag{A}$$

$$\ddot{p}_i(t) + 2\varsigma_i\omega_i\dot{p}_i(t) + \omega_i^2 p_i(t) = F_i(p_1(t),\dots,p_n(t)) + E_i(t) \tag{B}$$

$$C_i(\tau) = e^{-\omega_i\varsigma_{ef,i}\tau}\left(\cos\left(\omega_i\tau\sqrt{1-\varsigma_i^2}\right) + \frac{\varsigma_i}{\sqrt{1-\varsigma_i^2}}\sin\left(\omega_i\tau\sqrt{1-\varsigma_i^2}\right)\right) \tag{C}$$

Previous work has shown that the pressure oscillations can be described by a superposition of second order oscillators with a coupled forcing term F_i in addition to a random forcing term E_i.[8] The autocorrelation function can be solved analytically using Fourier analysis if the coupled forcing term in Eq. B is lumped with the damping coefficient ζ of that mode into an effective damping coefficient ζ_{ef}. This solution, Eq. C, has a decay envelope dependent on ζ_{ef}. As a result, the decay envelope of the calculated autocorrelation coefficient is a line in the logarithmic domain and ζ_{ef} can be extracted from the slope of that line. An example of autocorrelation data is shown in Figure 6 where the effects of the bandpass filter is seen as smoothing the autocorrelation function at a given instance in time, which allows an easier curve fit of the decay envelope.
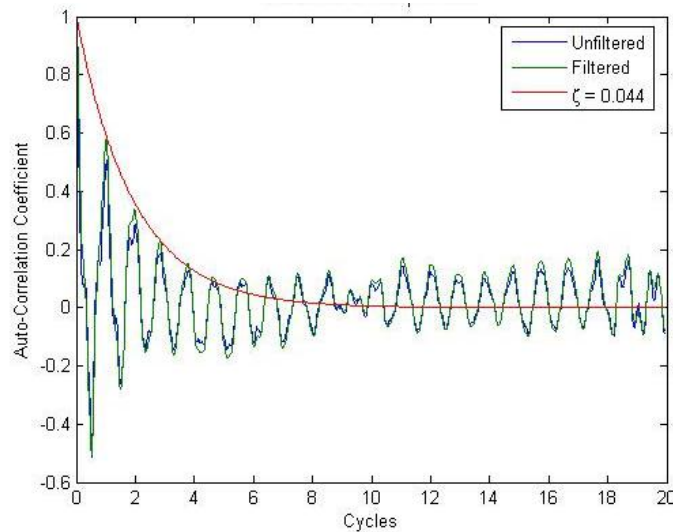

Figure 6. Curve fit of decay envelope of a filtered autocorrelation function for the 600 mm combustor for equivalence ratio of 0.42.

This particular curve fit is performed by a least mean square of the first ten local maxima of the absolute value of the autocorrelation function. From basic analysis of ordinary differential equations, one would expect that the amplitude of the pressure oscillation decreases and the damping coefficient increases. In Figure 7, we observe this expected trend with the effective damping coefficient ζ_{ef}, which is performed for several instances of time for each data set. In this data set, the combustor became increasingly unstable as the fuel/air ratio increased. However, the estimate of the damping coefficient is inherently noisy and, thus, different values were achieved for different portions of the same data. The bounding lines in this graph are the minimum, mean, and maximum effective damping coefficients. This implies that the effective damping coefficient can lead to incorrect conclusions if we use the instantaneous (noisy) ζ instead of a converged estimate. Examples of typical distributions are shown in Figure 8 and Figure 9 from the result of 300 calculations over a period of two seconds.
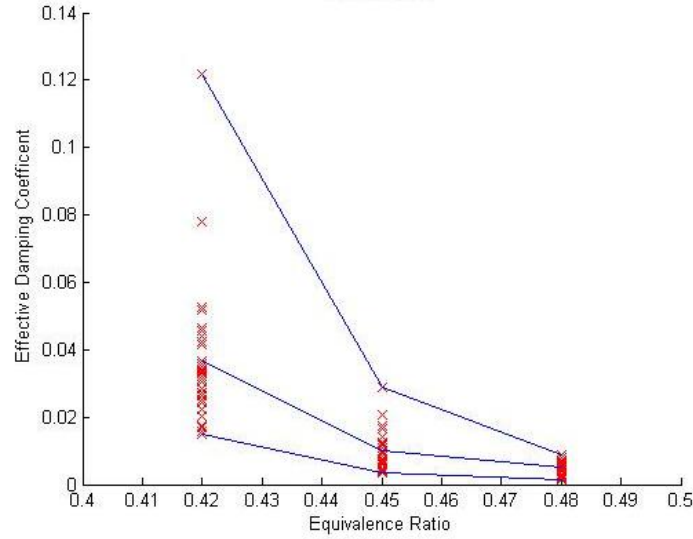
Figure 7. Distribution of damping coefficient for the 600 mm long combustor.
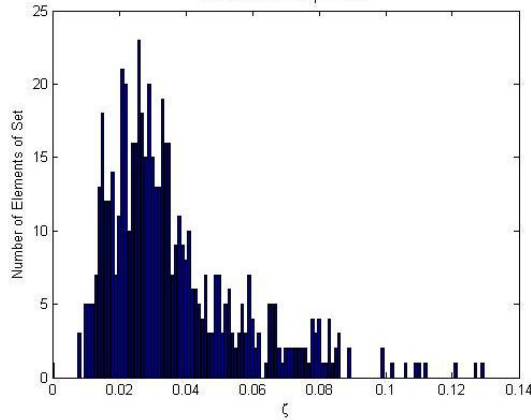
Figure 8. Distribution function for ζ for 600 mm combustor at $\varphi = 0.42$.

Figure 9. Distribution function for ζ for 300 mm combustor at $\varphi = 0.42$.

For further insight into convergence of the estimate, simulations were performed with a second-order oscillator under random forcing. This would allow a parametric study into understanding the effects of how we calculate the autocorrelation function on the estimate for the

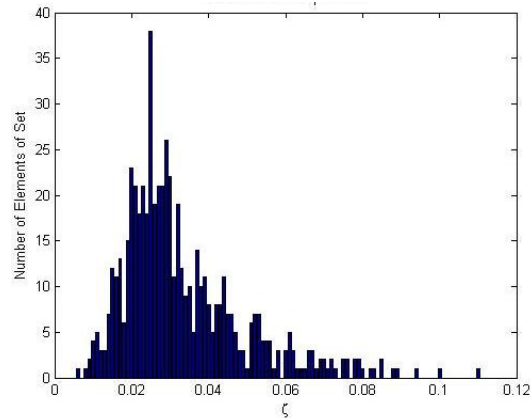effective damping coefficient as a function of instability frequency and actual damping coefficient. Of particular interest was the determination of an optimal period of integration to calculate the autocorrelation function and how many points to use in a curve fit of this data.

A typical result of this simulator using an instability frequency of 500 Hz for two different zetas is shown in Figure 10. This data shows an under prediction of the mean ζ, which was later traced to how the curve fitting is performed and is best illustrated if we reconsider Figure 6. The autocorrelation function is seen to "ring" (i.e., for its envelope to decrease to low values, but oscillate slightly) in its evaluated range due to persistent random forcing. As a result, the local maxima corresponding to the decay envelope are less representative as the dummy time variable τ is increased. This suggests the need to curve fit to less local maxima. In the case of using a curve fit with two points, the mean ζ can be accurately determined for $0.02<\zeta<0.3$. The standard deviation of the predicted ζ was found to scale inversely with $\sqrt{T}$, as can be seen in Table 1. The number of instability integration cycles corresponds to a multiple of the instability period T in Eq. 1. Anything below 100 cycles produces unreliable results. It can also be seen that at higher natural frequencies the error in observed mean ζ increased, which is attributed to the random forcing being simulated at a sampling frequency. This means that the forcing function, which should be discontinuous for all time, is actually continuous for an infinite number of time intervals corresponding to the sampling period. The spectrum of the forcing function is not perfectly broadband and hence this is an error that is associated with simulation and is not present in experimental evaluations.
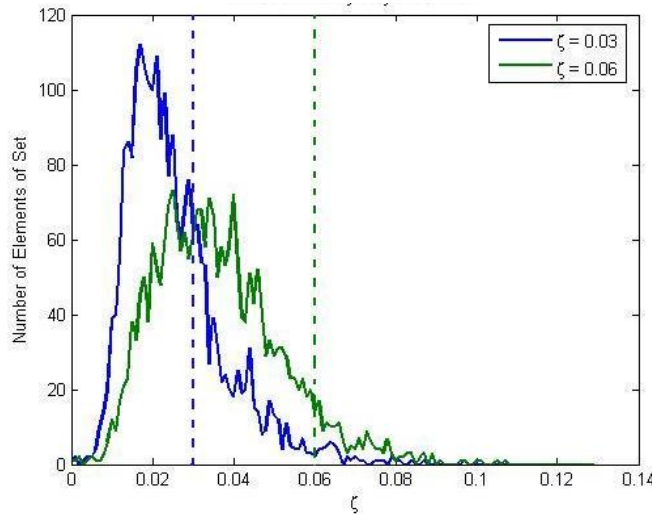
Figure 10. Comparison of extracted ζ with simulated ζ.

Table 1. Mean and standard deviations of ζ observed for a simulated mean ζ value of 0.03 with 10 kHz sampling frequency.

Frequency\N_{int}	100	315	1000
350	0.0279 | 0.0128	0.0293 | 0.0088	0.0292 | 0.0048
500	0.0269 | 0.0126	0.0280 | 0.0087	0.0277 | 0.0044
650	0.0246 | 0.0114	0.0248 | 0.0065	0.0247 | 0.0037

Overall, we have shown that a dynamic instability margin estimator can provide improved time response for an active instability margin management (AIMM) system, while maintaining sufficient accuracy in the margin estimate.

III.C Active Dynamic Instability Control

Active control has been demonstrated by various researchers to be a viable method of minimizing instability amplitudes. One of the key remaining fundamental issues is better understanding and modeling of the **factors that limit active controller effectiveness**. For example, in our lab, we have found that identical controllers work very differently under different conditions. As such, a key focus of the work has been to better understand the factors that influence active control effectiveness.

Active instability control is based upon reducing the amount of acoustic energy that accumulates within a system by increasing the damping. A linear analysis of the energy equation leads to the Rayleigh Criterion,[9] which states that acoustic damping is at its maximum when pressure perturbations are perfectly out of phase with heat release oscillations. Early controllers assumed that the heat release oscillations induced by fuel oscillations would be proportional. This led to simple adaptive phase shifting controllers where the fuel supply is forced at the frequency of the instability; however, the literature often shows a limit to controller effectiveness where the combustion instability is attenuated but not fully suppressed.

In prior annual reports the emphasis was placed on understanding the statistics of a controlled combustor's acoustic response in light of Rayleigh's Criterion. This approach required specifying the controller prior to the analysis. As a result, the statistical analysis developed earlier is able to show control trends but not explain them. Since then an alternative approach based upon system theory was implemented to circumvent this issue. This approach results in a set of integral constraints showing how a controlled system response is dependent upon the uncontrolled system response[10]. Once this theory is extended to handle time delays the results show that control is hindered by the presence of unstable open loop zeros from the heat release perturbations induced by fuel oscillations from the controller. Combustor designs that minimize this effect make the uncontrolled combustor increasingly unstable.

III.C.1   Model Development

To model this phenomenon, a stochastic wave description of combustion dynamics was developed (as outlined in our previous Annual Reports) detailing the interactions of multiple time delays with background noise.

$$\chi_n^{(5)}(t') + \omega_n'^2 \ddot{\chi}_n(t') + \left(\sum_{i=0}^{5} \sum_{m=1}^{\infty} C_{i,n,m} \frac{\partial^i \chi_m(t')}{\partial t'^i} \right) =$$

$$F_V'(t') + F_\phi'(t') + \sigma_n \xi_n(t') \tag{1}$$

$$F_V'(t') = -\frac{n_C}{\tau_V'} \sum_{m=1}^{\infty} \left[\left(\ddot{\chi}_m(t') - \frac{1}{\tau_V'} \left(\dot{\chi}_m(t') - \dot{\chi}_m(t' - \tau_V') \right) \right) \psi_n(x_f') \nabla' \psi_m(x_f') \right.$$

$$\left. -2M \left(\dot{\chi}_m(t') - \frac{\chi_m(t') - \chi_m(t' - \tau_V')}{\tau_V'} \right) \nabla' \psi_n(x_f') \nabla' \psi_m(x_f') \right]$$

(2)

$$F_\phi'(t') = -M \frac{n_C \beta^2}{\tau_V'} \left[-\frac{n_S}{\tau_V'(\beta^2 - 1)} \frac{\partial}{\partial t'} u(t' - \tau_A' - \tau_V') \psi_n(x_f') \right.$$

$$+\beta^2 \frac{(\beta^2 - 1)n_H + \beta^2 n_S}{\tau_V'(\beta^2 - 1)} \frac{\partial}{\partial t'} u\left(t' - \tau_A' - \frac{\tau_V'}{\beta^2} \right) \psi_n(x_f')$$

$$+\left((n_H + n_S) \frac{\partial^2}{\partial t'^2} u(t' - \tau_A') - \frac{(1 + \beta^2)n_S + \beta^2 n_H}{\tau_V'} \frac{\partial}{\partial t'} u(t' - \tau_A') \right) \psi_n(x_f')$$

$$+2\left(\frac{Mn_S}{\tau_V'(\beta^2 - 1)} u(t' - \tau_A' - \tau_V') - M(n_H + n_S) \frac{\partial}{\partial t'} u(t' - \tau_A') \right) \nabla' \psi_n(x_f')$$

$$+2M \frac{(1 + \beta^2)n_S + \beta^2 n_H}{\tau_V'} u(t' - \tau_A') \nabla' \psi_n(x_f')$$

$$\left. -2\beta^2 M \frac{(\beta^2 - 1)n_H + \beta^2 n_S}{\tau_V'(\beta^2 - 1)} u\left(t' - \tau_A' - \frac{\tau_V'}{\beta^2} \right) \nabla' \psi_n(x_f') \right]$$

(3)

Equation (1) is a non-dimensional system of stochastic delay differential equation (SDDE) for the temporal velocity mode amplitudes (χ) that has been normalized by the period of the fundamental frequency. The first two terms on the left hand side represent a standard harmonic oscillator that describes the amplitude dynamics of a given natural combustor mode. The final set of terms on the left hand side represents the effects of boundary conditions. On the right side the first two terms are heat release source terms for velocity and fuel perturbations, as detailed in Eq. (2) and Eq. (3). These two terms describe both the internal feedback loop responsible for instabilities, as well as the actions of the controller. Background noise forcing is represented by the final term on the right hand side. A graphical representation of Eq. (1) is shown in Figure 11. Details on the numerical values used for the coefficients in Eq. (1) throughout this report are contained in the appendix.

The main contribution of this new model is the incorporation of multiple time delays. In Figure 11 the time delays come from the internal feedback loop representing the self-excitation mechanism and the control feedback loop. These transfer functions are marked by the dashed teal box. Earlier models did not include the internal feedback loop or assumed that the self-excitation and control mechanism are the same.[11] The GaTech model allows for different excitation mechanism in both of these feedback loops. Multiple time delays can also appear in a single transfer function. Previous investigations assumed the existence of an *n-τ* heat release model[12] to ensure that the control feedback loop would only have a single time delay. This is possible if the feedback control mechanism is a loud speaker with the additional assumption of a

low Strouhal number flame; however, in the more practical case of using fuel perturbations as the control mechanism recovering an *n-τ* heat release model is impossible.[13] The GaTech model removes this commonly used incorrect assumption and uses heat release perturbation models derived from first principles.[13]
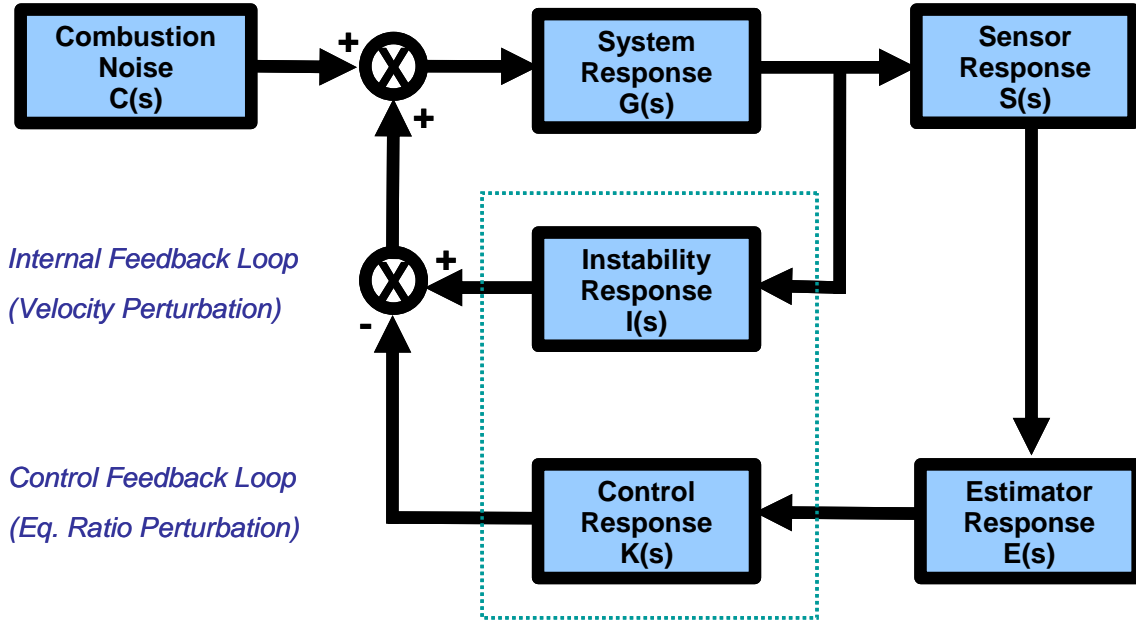

Figure 11. Feedback diagram.

III.C.2   Rayleigh's Criterion[14]

Feedback control of combustion instabilities work by modifying the balance of acoustic energy, Eq. (4), inside a combustor.

$$\frac{\partial E_2}{\partial t} + \nabla \cdot I_2 = \frac{\gamma - 1}{\gamma p_0} p_1 \frac{\partial q_1'''}{\partial t} \tag{4}$$

Equation (4) shows that the rate of change of acoustic energy, E_2, is equal to the difference of the acoustic energy flux, I_2, with an acoustic energy generation/dissipation term that depends upon perturbations in the pressure field, p_1, and volumetric heat release rate, q_1'''. This is called the Rayleigh source term. When these perturbations are cyclical (in phase within 90º) they act as an acoustic energy source, but when they are anti-cyclical they act as a sink of acoustic energy. Based upon observations from Johnson et al.[15] that the instability phase behaved erratically as the instability amplitude was suppressed by active control, it was hypothesized that active controllers interact with the combustion dynamics in such a way that increases the rate of phase drift in a combustion instability. As a result the observer responsible for phase tracking would feed increasingly inaccurate information to the controller. The phase mismatch between the actual optimal phase and estimated optimal phase reduces the active controller effectiveness of satisfying Rayleigh's Criterion to the point that the controller authority saturates.

Test data provided by NASA Glenn related to the work of Kopasakis et al.[16] helped lend credence to this idea. The basic premise follows work by Lieuwen[17] that calculates the mean squared phase drift per cycle using a discrete time Markov model. The results of applying this model to the NASA Glenn data are given by Table 2; the discrete time Markov model fits the NASA Glenn data well with correlation coefficients greater than 0.95. Of particular interest is the change of mean squared phase drift with control effectiveness. As the maximum pressure perturbations are suppressed the mean squared phase drift per cycle increases. A stark difference can be seen when comparing closed loop control with the open loop controllers. The closed loop controllers, while more effective, greatly aggravates the mean squared phase drift per cycle.

Table 2. NASA Glenn Test Results

NASA GRC Control Case	Max Pressure Perturbation (psi)	Mean Squared Phase Drift per Cycle (deg^2/cycle)	Correlation Coefficient
No Control	18.4	14.8	0.990
Closed Loop at Fundamental	13.1	1330	0.997
Closed Loop at 1st Harmonic	8.59	1740	0.981
Weak Open Loop at 200 Hz	18.2	24.1	0.992
Strong Open Loop at 200 Hz	16.6	69.7	0.967
Open Loop Forcing at 289 Hz	16.9	23.5	0.962

To develop deeper insight into the results of Table 2, we decided to use the Fokker-Planck equation[18] which solves for the time varying probability density function response (pdf). Once the pdf of the system response is known the statistics of the phase drift rate can be calculated. This was successfully accomplished for a second order oscillator forced by white noise; however, attempts to extend these results for time delayed systems failed. The Fokker-Planck equation assumes Markovian (memoryless) behavior. A time delayed system requires the knowledge of past states to predict the future. As a result, we abandoned the Fokker-Planck approach to focus on more viable analytical techniques. To simplify analysis, the focus became identifying what limits control effectiveness when full state information is available, as a stepping stone to the mixed control/estimation problem. Since the phase drift rate hypothesis is related to state estimation, this was put aside.

III.C.3   **Statistical Analysis**

The thermo-acoustic model detailed by Eq. (1) is a linear system with a Gaussian input which ensures that the output is Gaussian.[19] As a result, only the mean vector and the covariance matrix are needed to completely define the probability density function (pdf) of χ and all of its derivatives. If Eq. (1) is exponentially stable then the steady state mean is zero. The steady state covariance matrix can be found by taking the inverse Fourier transform of the power spectral matrix which is found by taking the Fourier transform of Eq. (1) and multiplying by its complex conjugate.[20] Going forward the modes of χ will be normalized by the natural frequency, ω_n, of that mode. Throughout the rest of this document, the new random variables X and Y will refer to the modes of χ and their normalized derivatives, respectively.

If Eq. (1) is truncated to a single mode the ratio of the variances of *Y* and *X* is actually the ratio of the mean acoustic potential energy to the mean acoustic kinetic energy.[20]

$$\frac{\langle \text{P.E.} \rangle_n}{\langle \text{K.E.} \rangle_n} = \frac{\sigma_{(y,n)}^2}{\sigma_{(x,n)}^2} \tag{5}$$

If this ratio is less than one, then the majority of the acoustic energy in that mode is acoustic kinetic energy and vice versa. In the limit of no heat release this ratio is one since this recovers the classical acoustic limit where the equi-partition of acoustic energy is valid.[21] Deviations from an equi-partition of acoustic energy will prove to be crucial to describing and understanding the steady state pdf response of Eq. (1).

Using a Kryloff and Bogoliuboff decomposition[22] given by Eq. (6) and Eq. (7) the random variables X_n and Y_n can be converted into random variables for amplitude, R_n, and a total phase, θ_n, defined by Eq. (8) and Eq. (9).

$$X_n(t) = R_n(t)\sin\left(\theta_n(t)\right) \tag{6}$$

$$Y_n(t) = R_n(t)\cos\left(\theta_n(t)\right) \tag{7}$$

$$R_n(t) = \sqrt{X_n^2(t) + Y_n^2(t)} \tag{8}$$

$$\theta_n(t) = \arctan\left(X_n(t)/Y_n(t)\right) \tag{9}$$

The marginal pdf for amplitude and total phase for Eq. (1) truncated to a single mode is given by Eq. (10).

$$f(R_n,\theta_n) = \frac{R_n}{2\pi \sigma_{(x,n)}\sigma_{(y,n)}}\exp\left[\frac{-\left(\sigma_{(x,n)}^2\cos^2\theta_n + \sigma_{(y,n)}^2\sin^2\theta_n\right)R_n^2}{2\sigma_{(x,n)}^2\sigma_{(y,n)}^2}\right] \tag{10}$$

In the limit of no heat release perturbations, amplitude and total phase are independent random variables represented by a Rayleigh and circular uniform pdf respectively.

$$f(R,\theta) = \frac{R}{2\pi\sigma^2}\exp\left[\frac{-R^2}{2\sigma^2}\right] \tag{11}$$

When the ratio of the variances in Eq. (5) is unity, then Eq. (11) is recovered. Generally, the amplitude and phase pdf's are not independent for time delayed or coupled systems.

More explicit results can be obtained for the individual marginal pdf's of amplitude and total phase. A marginal pdf of the total phase comes from integrating over the region of support for the amplitude in Eq. (10).

$$f(\theta_n) = \frac{\sigma_{(x,n)}\sigma_{(y,n)}}{2\pi}\left(\sigma_{(x,n)}^2 \cos^2(\theta_n) + \sigma_{(y,n)}^2 \sin^2(\theta_n) \right)^{-1} \tag{12}$$

If the ratio of the variances is unity, then the marginal pdf of the total phase is a circular uniform distribution as expected. Figure 12 shows the total phase pdf for this case, as well as cases where this ratio is less than and greater than unity to illustrate what happens when acoustic potential and acoustic kinetic energy are not equi-partitioned. Deviations from the equi-partition of generalized energy create regions of preferential total phase. When more acoustic kinetic energy is present than acoustic potential energy the total phase prefers to avoid regions that are multiples of π. This increases the probability that $|\sin(\theta_n)|$ is as large as possible while ensuring that $|\cos(\theta_n)|$ is as small as possible. In turn, this implies that the fluctuations in the oscillator's instantaneous values, Eq. (6), are larger than the fluctuations in its rate of change, Eq. (7), as expected. Similarly, the situation is reversed when more acoustic potential energy exists than acoustic kinetic energy, resulting in the total phase preferring regions that are multiples of π.
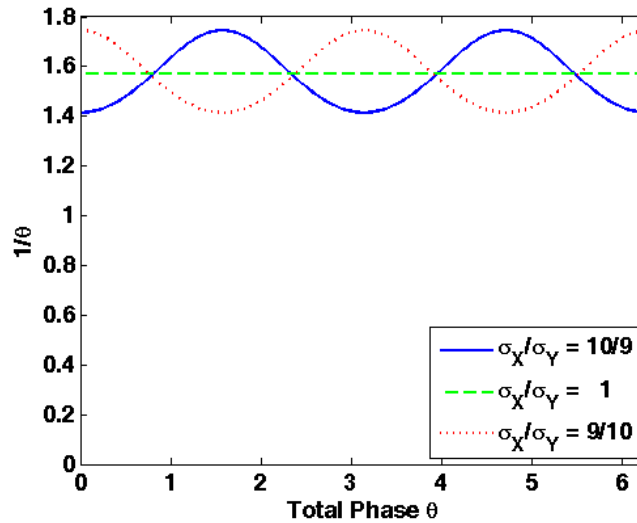

Figure 12. Total phase pdf for varying ratios of acoustic kinetic energy and acoustic potential energy.

Integrating Eq. (10) over the region of support for the total phase yields a Hoyt distribution for the amplitude pdf.

$$f_{R_n}\left(q = \frac{\sigma_{(y,n)}}{\sigma_{(x,n)}}, w = \sigma_{(x,n)}^2 + \sigma_{(y,n)}^2 \right) = \frac{(1+q^2)}{qw} R_n \exp\left(-\frac{(1+q^2)^2 R_n^2}{4q^2 w} \right) I_0\left(\frac{(1-q^4)R_n^2}{4q^2 w} \right) \tag{13}$$

Two parameters fully describe this pdf: the shape parameter q is determined by the amount of deviation in the equi-partition of acoustic energy; while the spread parameter w is determined by the total acoustic energy in that mode. Exploring the statistics of the marginal amplitude pdf described by Eq. (13) can also be insightful. In these expressions E represents the complete elliptical integral of the second kind.

$$\langle R_n \rangle = \sqrt{\frac{2}{\pi}} \sigma_{(x,n)} E\left(1-q^2\right) = \sqrt{\frac{2w}{\pi\left(1+q^2\right)}} E\left(1-q^2\right) \tag{14}$$

$$\langle R_n^2 \rangle = \sigma_{(x,n)}^2 + \sigma_{(y,n)}^2 = w \tag{15}$$

$$E(\kappa) = \int_0^{\frac{\pi}{2}} \sqrt{1-\kappa\sin^2\theta}\, d\theta \tag{16}$$

These expressions show a strong dependence upon w. In fact, w is exactly the second moment of amplitude given by Eq. (15). Another useful statistical figure of merit is the coefficient of variation, c_v, which describes the ratio of the standard deviation to the mean of a variable.

$$c_v(R_n) = \frac{\sqrt{\mathrm{Var}(R_n)}}{\langle R_n \rangle} = \frac{\sqrt{\frac{\pi}{2}\left(1+q^2\right) - E^2\left(1-q^2\right)}}{E\left(1-q^2\right)} \tag{17}$$

As this coefficient increases, which solely depends on q, the probability that the amplitude will deviate from its mean is increased, as is plotted in Figure 13. For convenience, the abscissa has been normalized such that it belongs to the set [0,1] instead of [0,∞). A minimal value of $\sqrt{(4/\pi-1)}$ is found for the coefficient of variation when the ratio of the variances is one, corresponding to one half in the normalized coordinate, and reaches a maximum value of $\sqrt{(\pi/2-1)}$ at the boundary points. Clearly, Figure 13 is symmetric and monotonically increasing as deviations from equi-partition of energy increase.
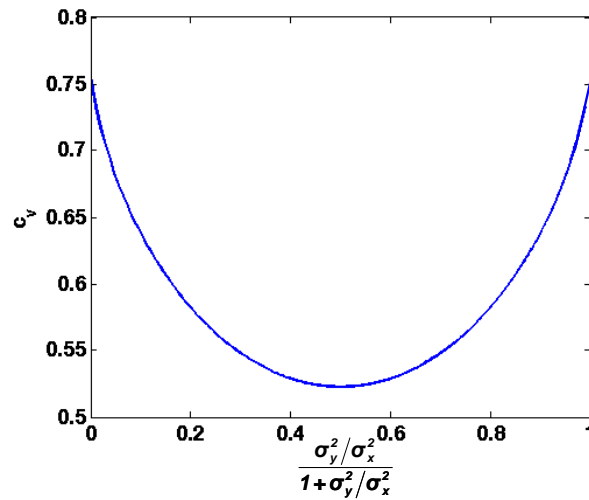

Figure 13. Coefficient of variation as a function of the ratio between acoustic potential energy and acoustic kinetic energy.

III.C.4   Spectral Analysis

One of the shortcomings of the statistical method was the computation time required to check if Eq. (1) was stable before requiring another lengthy computation for the statistics of χ. For a linear SDDE, stability is determined by the stability of the mean equation,[23] which gives a delay differential equation (DDE). Linear DDE's are stable as long as the rightmost eigenvalue, called the spectral abscissa, is contained in the left hand complex plane.[24] The spectral abscissa is also used as a measure of stability in control theory. While this is not a direct replacement for system performance, the trends in the spectral abscissa tend to follow those of system performance. The eigenvalues of a DDE can be found with a pseudospectral method to discretize the delay.[25]
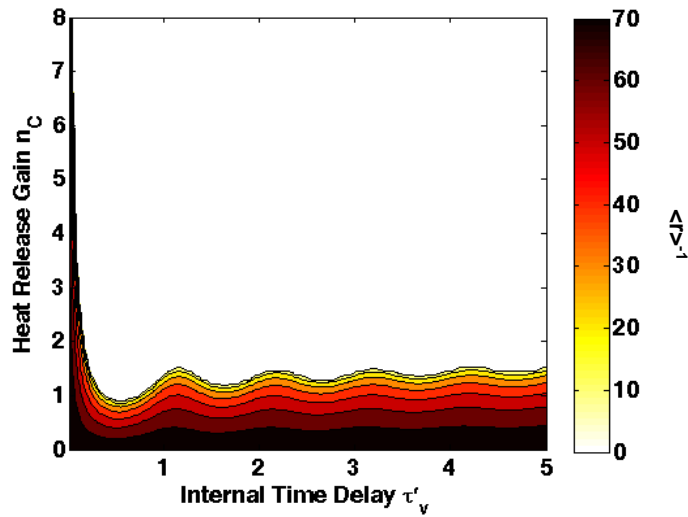

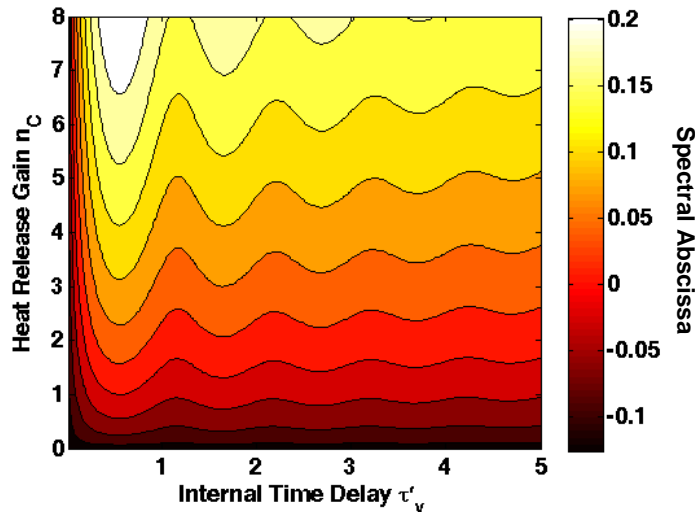Figure 14. Inverse of mean amplitude response for an uncontrolled self-excited combustor.

Figure 15. Spectral abscissa for an uncontrolled self-excited combustor.

In Figure 14, a parameter mapping of the performance of an uncontrolled self-excited combustor is shown using the statistical method detailed in a previous annual report while Figure 15 shows the exact same parameter map based upon the spectral abscissa. The stability boundaries and the trends are exactly the same in both figures. This shows that calculations based upon the spectral abscissa are a reasonable engineering analysis tool. An additional benefit of using the spectral abscissa is that it can provide information about unstable operating conditions. The deeper the spectral abscissa is in the right hand plane the harder a control system will have to work to stabilize the system.

In addition to stability and performance, another concern is system robustness. A controlled combustor needs good off-design performance to compensate for unmodeled combustion dynamics or poorly known coefficients in Eq. (1). When the parameters of a system are perturbed, the location of the eigenvalues will move. One way to investigate the propensity of eigenvalues to move is through pseudospectra,[26] which are calculated by evaluating the characteristic equation of Eq. (1) over the entire complex plane. This is reproduced in Eq. (18) below where $\mathbf{a}$ is the infinitesimal generator[27] of Eq. (1).

$$\Lambda_\varepsilon(\mathbf{a}) = \left\{ s \in \mathbb{C} : \left\| (s\mathcal{T} - \mathbf{a})^{-1} \right\| \geq \varepsilon^{-1} \right\} \tag{18}$$

There are many different equivalent definitions for the pseudospectra. In Eq. (19) contours of the pseudospectra are revealed to contain the set of all possible eigenvalues of the infinitesimal generator with respect to perturbations less than ε; thereby creating a very powerful tool to visualize the robustness of a self-excited combustor. Such a contour plot is shown in Figure 16 below.

$$\Lambda_\varepsilon(\mathbf{a}) = \left\{ \exists : \left\| (\Delta\mathbf{a}) \right\| \leq \varepsilon : s \in \Lambda(\mathbf{a} + \Delta\mathbf{a}) \in \mathbb{C} \right\} \tag{19}$$

The eigenvalues from Eq. (1) are shown to have a strong propensity to drift into the right hand complex plane for small perturbations. From a control system point of view the robustness of the system is a serious concern and needs to be addressed in addition to the system performance at the design point.
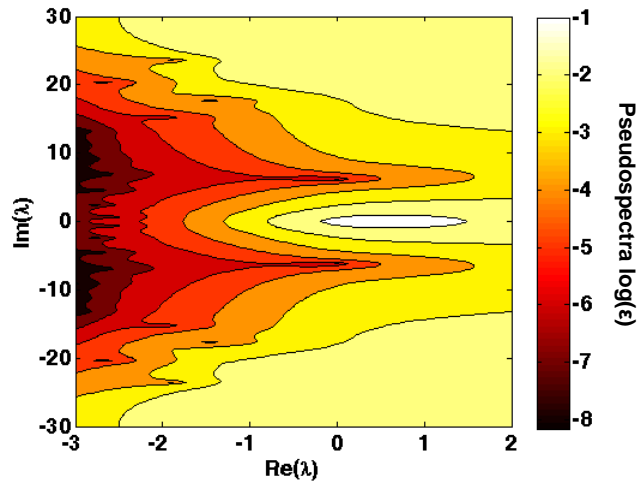

Figure 16. Pseudospectra of a self-excited combustor.

Constraints on Controlled Combustor Response

In control theory the very presence of a feedback loop creates frequency response constraints in the closed loop system dynamic.[10]   A general feedback diagram for a single input single output (SISO) system is used to study these constraints is shown in Figure 17. Here, a reference signal $R(s)$ is fed into the plant transfer function $P(s)$. An ideal sensor $Y(s)$ reads the output of $P(s)$ plus any system disturbances $D(s)$. $Y(s)$ plus any noise $N(s)$ that exists in the sensor is the input to the compensator $F(s)$. Afterwards, the compensator output is fed back into $P(s)$.
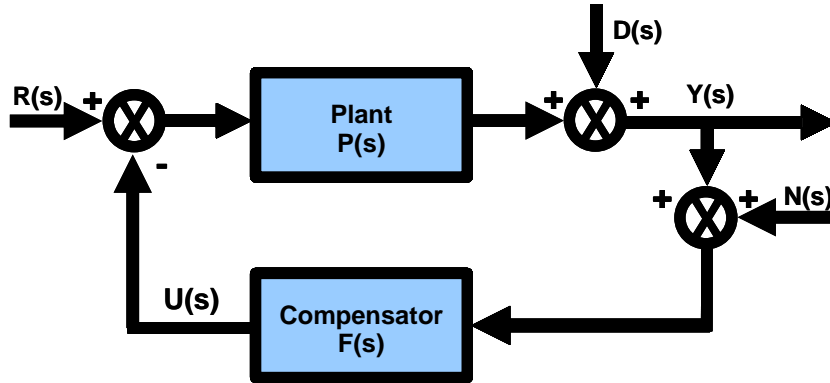

Figure 17. General SISO feedback diagram.

Before proceeding, the feedback diagram that physically illustrates self-excited, noise driven, combustors, Figure 11, needs to be understood in the context of Figure 17. The plant $P(s)$ is the closed loop transfer function of the internal feedback loop which includes the transfer functions of the combustor $G(s)$, the self-excitation due to velocity perturbations $I(s)$, and the sensor $M(s)$ while the compensator $F(s)$ includes the effects of an estimator $E(s)$, if present, and the control response $K(s)$ due to equivalence ratio perturbations. All of the input terms in Figure 17 are present in Figure 11 except for the reference signal $R(s)$, which can be interpreted as driving from combustion noise $C(s)$. When trying to write an expression for the closed loop response $Y_r(s)$ in the absence of disturbances and sensor noise the sensitivity function $S(s)$ naturally crops up.

$$Y_r(s) = S(s)P(s)R(s) \tag{20}$$

$$S(s) = \left[I_n + L(s) \right]^{-1} \tag{21}$$

$$L(s) = P(s)F(s) \tag{22}$$

The sensitivity function defined in Eq. (21) is the transfer function between output disturbances $D(s)$ and the system output. It happens to be a function of the open loop transfer function $L(s)$ which is a mapping between the plant input and the controller output. This means that open loop performance given by Eq. (22) can be related to closed loop performance given by Eq. (20) via the sensitivity function from Eq. (21).

Another important function is the complementary sensitivity function $T(s)$, defined by Eq. (24), which can be interpreted as the transfer function between sensor noise $N(s)$ and the system output.

$$Y_n(s) = -T(s)N(s) \tag{23}$$

$$T(s) = L(s)\left[I_n + L(s)\right]^{-1} \tag{24}$$

The complementary sensitivity function can also be viewed as the transfer function between the reference signal $R(s)$ and the control input $U(s)$ in the absence of output disturbances and sensor noise.

$$U(s) = T(s)R(s) \tag{25}$$

While the sensitivity function has a strong connection to system performance the complementary sensitivity function has a strong connection to the robustness of the system. On the $j\omega$-axis the magnitude of $T(s)$ at a given frequency decides the bounds on the system's unstructured multiplicative uncertainty $M(\omega)$ at that frequency.[28]

$$\left|T(j\omega)\right| < \frac{1}{M(\omega)} \tag{26}$$

Inspection of the definition of the sensitivity function from Eq. (21) and its complement defined by Eq. (24) reveal that their sum must equal one which is called an algebraic constraint.

$$S(s) + T(s) = 1 \tag{27}$$

This shows that in any control design, an inevitable tradeoff exists between system performance and robustness at the same frequency. At high frequencies, where modeling is the least accurate and robustness is most needed, $|T(j\omega)|$ is required to be very small, but in that limit $|S(j\omega)|$ is near one. Meanwhile, at low frequencies where $P(j\omega)$ is large, $|S(j\omega)|$ is required to be very small to get good performance, but in that limit $|T(j\omega)|$ is near one. Taken together, these two design goals do not interfere as long as the frequency range where good performance is needed does not overlap with the frequency range where robustness is needed. Sometimes the system performance and robustness can both be poor at the same frequency when both $|S(j\omega)|$ and $|T(j\omega)|$ are greater than one.

Design constraints can also exist across different frequencies and are expressed as integral constraints. A set of these constraints specific to Eq. (1) are given by Eq. (28) to Eq. (31) below.[20]

$$\int_0^R \log\left|S(j\omega)\right| d\omega = \pi \sum_{i=1}^{n_p} \mathrm{Re}(p_i) + const \tag{28}$$

$$\int_0^R \log\left|T(j\omega)\right| d\omega = \pi \sum_{i=1}^{n_p} \mathrm{Re}(z_i) + const \tag{29}$$

$$\int_0^\infty \log\left|S(j\omega)\right| \frac{d\omega}{\omega^2} = \pi \sum_{i=1}^{n_p} \frac{1}{p_i} \tag{30}$$

$$\int_0^\infty \log\left|T(j\omega)\right|\frac{d\omega}{\omega^2} = \pi\sum_{i=1}^{n_z}\frac{1}{z_i} + \frac{\pi}{2}\tau'_A \tag{31}$$

Equation (28) and Eq. (29) are the Bode integral constraints for the sensitivity function and its complement. They reveal that unstable poles (p_i) and zeros (z_i) of $L(s)$ deep inside the right hand complex plane are bad for performance and robustness. Equation (30) and Eq. (31) are modified forms of the Bode integral constraints which show that poles and zeros should also be kept from approaching the $j\omega$-axis from the right hand complex plane. Large delays in the control system are also seen to contribute to reducing the robustness of a control system.

III.C.5   Results

A commonly used framework to evaluate the performance of a control system is a quadratic cost function such as one given by Eq. (32) where the first term represents the amount of acoustic energy in the combustor while the second term represents the control effort.

$$J = \int_0^\infty \left\langle \vec{x}(t'), \mathcal{Q}\vec{x}(t')\right\rangle + \left\langle \vec{u}(t'), \mathcal{R}\vec{u}(t')\right\rangle dt' \tag{32}$$

Mathematically, if the control engineer was indifferent to the control effort the acoustic energy in the combustor could be reduced to a predetermined level; however, real fuel actuators in a combustor have constraints on their bandwidth and actuation authority[29]. As a result, there are limits to the control engineer's ability to reshape the acoustic energy inside a combustor. These limits are also influenced by the feedback structure of the controlled self-excited combustor. This allows the cost function to be bounded from above by the sensitivity function and its complement in Eq. (33).[20]

$$J \leq \int_0^\infty \left\|\mathcal{Q}\right\|_2 \left\|S(j\omega)P(j\omega)R(j\omega)\right\|_2^2 + \left\|\mathcal{R}\right\|_2 \left\|T(j\omega)R(j\omega)\right\|_2^2 d\omega \tag{33}$$

This bound shows that the cost function depends on two terms. The first item represents how far the controller has to move the unstable open loop poles to their closed loop position while the second term reveals the difficulty (amount of control effort) of moving these unstable open loop poles, which depend upon the unstable open loop zeros. What limits control effectiveness is dictated by how given combustor designs distribute their unstable open loop poles and zeros. If we refer back to Figure 11 the open loop poles come from the combustor response $G(s)$ and the self-excitation mechanism $I(s)$ while the open loop zeros come from the control system $K(s)$. Physically, these poles and zeros come from the combustor geometry and how the flame is stabilized.

From a design point of view the dependent variables in shaping the zeros of Eq. (1) are the flame geometry factor β and the internal time delay τ'_v which dictates the mean flame shape (see appendix for details). Figure 18 shows how the logarithm of the sum of all of the unstable open loop zeros depend on these factors. The logarithm does not naturally show up on the right hand side of the integral constraints in Eq. (29) but allows for easily interpretable contour plots. Inspection of Figure 18 immediately shows that unstable open loop zeros always exists in an equivalence ratio modulation based controller; otherwise, the contour plot would have values going to negative infinity. This is a terrible property for a control system because at high gains

the roots of the closed loop transfer function will migrate towards the zeros of the open loop transfer function[30]. As a result, high gain controllers are always destabilizing which create robustness problems for controllers that are prone to high gains, such as adaptive controllers.[31] Additionally, a control system seems to respond better at low flame geometry factors and high internal time delays. Physically, this corresponds to a long flame which pushes the position of mean heat release away from the combustor inlet. This acts like a free gain multiplier in the control system without increasing the control cost.
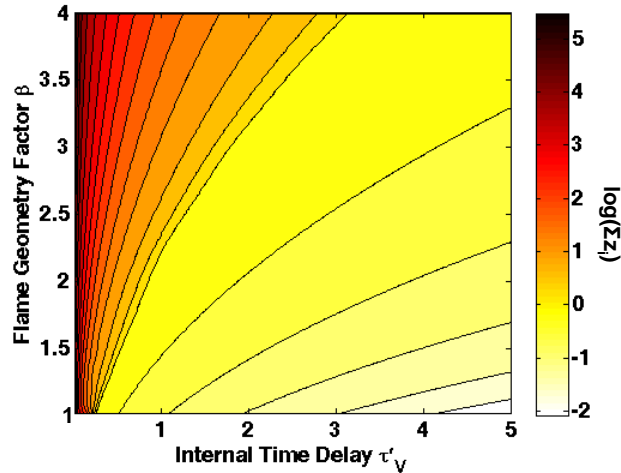

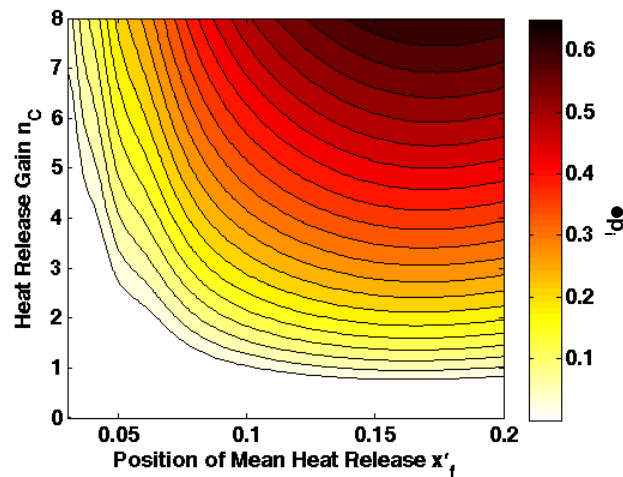Figure 18. Unstable zeros of a self-excited combustor.

Figure 19. Unstable poles of a self-excited combustor.

A good question to ask is how the unstable open loop poles are affected by changes that improve the location of the unstable open loop zeros. In Eq. (1) the zeros are indifferent to many of the parameters in the thermo-acoustic model but the poles are not. What really matters is how

the velocity perturbation self-excitation mechanism depends on the position of mean heat release. Just like the equivalence ratio modulation case, the volumetric heat release rate perturbations due to velocity disturbances also increases because the effective gain of the internal feedback loop is increasing as the position of mean heat release moves away from the combustor inlet. This can be seen in Figure 19 where the sum of the unstable open loop poles is seen to be increasing as x'_f and n_C increases.

A very interesting situation is created since the unstable poles and zeros follow the same trends. The unstable open loop zeros are much more sensitive to the position of mean heat release which is shown by the necessitation of the logarithm to plot meaningful contours in Figure 18 but not in Figure 19. As a result, by increasing the position of mean heat release the upper bound on the control cost in Eq. (33) due to the unstable open loop zeros decreases faster than the upper bound on the state cost due to the unstable open loop poles. These behavioral trends in the upper bound on the cost function suggest that the combustors most responsive to control are the ones most likely to be intrinsically unstable. This means that if the control engineer designed a control system for two different combustors, one stable and the other unstable, then the controlled unstable combustor will have better disturbance rejection than the controlled stable combustor.

III.C.6   Recommendations

Current combustors are not designed to be unstable nor will they be in the near future as long as the thermo-acoustic models are unreliable. Certain physical processes are not well understood or properly experimentally validated and certain tools for time delay system are not fully developed. Why design a combustor to be unstable but responsive to control if the control performance cannot be predicted ahead of time? Without this capability, performance and stability cannot be guaranteed.

The poor robustness qualities of time delay systems place stronger demands on the thermo-acoustic modeler. As a result, reduced order models for controlling combustion instabilities need to be quite detailed. Getting the phase information at high frequencies correct is very important to accurately model stability because of uncertain time delays. Most robustness tools for time delay systems are related to the small gain theorem[32] used for magnitude uncertainty although some work exists on extending passivity concepts for phase uncertainty to alleviate these difficulties.[33] At the very least, enough information about modeling deficiencies need to be known to set up a structured uncertainty problem so that the control engineer does not have to include an excessive amount of conservatism in their designs. This pushes the complexity of the required physics and the mathematical tools needed to make useful predictions. While other important factors exists that are responsible for limiting control effectiveness, particularly behavioral constraints on the fuel actuator, these factors will remain secondary as long as the effects of their idealized counter parts cannot be predicted and consistently reproduced.

The sensitivity analysis shows that three items are important in correctly predicting system performance: the unstable 1) poles and 2) zeros of the open loop transfer function; along with the 3) magnitude of the time delays. Of these three items the position of the unstable zeros is by far the most sensitive which means that the thermo-acoustic modeler should focus on improving and understanding the terms that they come from. For the combustion engineer this

means developing more elaborate volumetric heat release perturbation models and experimentally validating them. The control engineer can look at more complex sensitivity integral constraints, especially for multiple input multiple output (MIMO) systems.[34] Modal coupling in the heat release and acoustic boundary conditions are also sources of zeros that need to be understood but are currently unexplored. Alternative integral constraints exist for concepts such as passivity[35] and the mutual information rate[36] which could also lead to new insight.

III.D   Active Static Stability Control

Combustor static instability margin sensing based on identification of flame partial extinction and re-ignition events in optical and acoustic radiation produced during combustion has been demonstrated in premixed gas-fueled and non-premixed liquid-fueled swirl combustors at atmospheric pressure.[37-40] The extinction and re-ignition events, called LBO precursors were observed to occur more frequently as combustor's stability margin ($\Phi-\Phi_{LBO}$ or Φ/Φ_{LBO}) was reduced. Hence average occurrence rate of precursor events provides a measure of proximity of combustor to its blowout. Other approaches for LBO proximity sensing have also been proposed, including methods based on: 1) the standard deviation of the naturally occurring optical emission[41] and 2) the relative spectral power at low frequencies, in the naturally occurring acoustic radiation[42] or the combustor gas temperature determined from a diode-laser absorption measurement.[43]

LBO margin sensing studies, until now, were conducted under dynamically stable operating conditions. However, as lean combustion often has pronounced dynamic instabilities, one of the objectives of this work is to **investigate LBO margin sensing in the presence of dynamic instability**. Existence and detection of precursor events in the presence of high amplitude dynamic instability, having two types of instability mechanisms, i.e., flame-acoustic interactions and equivalence ratio oscillations is examined for LBO margin sensing.

Most of the previous LBO margin sensing studies have been performed at atmospheric pressure under less than realistic engine operating conditions. Similarly, most of previous work involved premixed, gas-fueled combustors. Therefore, another objective of this work is to **examine LBO precursor sensing at elevated pressure and temperature in a liquid-fueled, low NO$_x$ turbine engine combustor design called Lean Direct Injection (LDI)**.

III.D.1   Experimental Facilities

LBO sensing and the behavior of LBO precursors are examined in two distinctly different setups. The first is a gas-fueled (natural gas) combustor similar to low NOx premixed ground-power gas turbine combustors. The second is a liquid-fueled Lean Direct Injection (LDI) combustor more representative of next-generation low NOx aeroengine combustors.

Gas Fueled Atmospheric Rig

In order to study LBO sensing in the presence of combustion dynamics, a model combustor similar to lean premixed gas turbine engine combustors is chosen. The combustor is an atmospheric-pressure, swirl-stabilized dump combustor, schematically shown in Figure 20. Air enters the combustor through a choked valve in order to isolate the air supply from

combustor disturbances, specifically pressure oscillations. The air passes through a 22 mm diameter tube, in which two axial swirlers are located. The first swirler has a vane angle of 35°, while the second has a higher vane angle of 50°. The inlet also incorporates a 10 mm diameter (cylindrical) center-body for enhanced flame stabilization. The combustor is formed from a quartz tube, 70 mm in diameter and 0.6 m long.

One of the requirements of the combustor is to have combustion instabilities in lean conditions near blowout. The combustor is configured to have combustion instabilities of two kinds (flame-acoustic interactions and equivalence ratio oscillations) by having two types of fuel injection schemes. Gaseous fuel (natural gas or methane) can be injected into the air stream either far

Figure 20. Atmospheric pressure gas fueled rig.

upstream before the choked orifice or just upstream of the second swirler. By injecting fuel before the choked orifice, pressure perturbations cannot excite fuel-air ratio oscillations. In addition, the large distance between the combustor and the injection location promotes fuel air mixing. In the second method, fuel enters air stream between the two swirlers (68 mm upstream of the dump plane), through un-choked multiple injection orifices. This is intended to achieve substantial premixing, while still allowing for feedback from the combustion dynamics to perturb the fuel-air ratio. However, due to the small residence time between fuel injection and combustion there could be stratification in the mixture.

Nominal cold flow axial velocity in the combustor is 4.5 m/s, and the nominal combustor power is ~32 kW (0.11 MBTU/hr). Based on complete combustion and no heat losses, the bulk average exit axial velocity of the product gases would be 23 m/s. A fused silica optical fiber, with a cone angle of 24° was used for collection of optical emissions from the combustor. With the fiber located 6 cm from the center of the combustor, the optical detection region extends across the width of the combustor and 2.3 cm in the axial direction. The optical radiation first passes through an interference filter centered at 308 nm corresponding to OH[*] emission. A miniature metal package photomultiplier (PMT, Hamamatsu H5784-04), with a built-in amplifier, is used to detect the optical signal. Acoustic radiation from the flame is monitored with a condenser microphone (Bruel and Kjaer type 4939, flat frequency response up to 40 kHz) located 30 cm above and 50 cm radially offset from the center of the combustor exit.

Liquid Fueled High Pressure Rig

As noted previously, this work employs an LDI type combustor. Regarding the appropriate operating conditions, the question of what can be considered realistic operating conditions arises. For example, one can consider ground level (take off) or cruise conditions. A
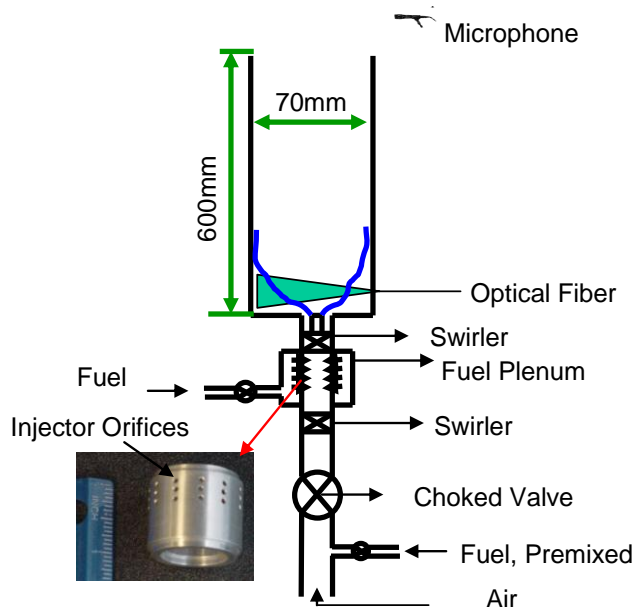
motivating aspect of the current work is low NOx engines for future supersonic passenger aircraft, which would operate at high altitudes (stratosphere). For cruise flight at high altitudes (~60,000 ft), combustor inlet pressures are estimated to be ~2-5 atm, and inlet temperature would be around 600 K even for large compression ratio engines, e.g., compressor pressure ratio of 40. Hence in the present work, a LDI combustor operating nominally at ~2-4 atm and inlet temperature of ~700 K is used.

The LDI injector used in the experiments is a single element configuration of a 9 element LDI injector, developed by NASA Glenn Research Center.[44] The multi-element injector has nine air swirlers with a fuel injector in the middle of each swirler in a 76.2×76.2 mm^2 overall area. In the present injector configuration, only the center injector is present and the surrounding injectors are replaced by co-flowing air, using a perforated sheet.

A cross sectional view of the LDI injector, with a quartz combustor liner is shown in Figure 21(a). The swirler has helical axial blades with a vane angle of 60°, and a theoretical swirl number of 1.02. The fuel nozzle employs a simplex, pressure-swirl atomizer. A converging-diverging venturi is used with both converging and diverging sections having a 40° angle. The venturi has a nominal exit diameter of 22 mm. The tip of the fuel nozzle is located nominally at the throat of the venturi. A cylindrical quartz tube with a diameter of 80 mm acts as combustor liner. In order to simulate the effect of surrounding injectors, which are absent in the single-element configuration, a perforated sheet with 2.38 mm diameter holes is used. The LDI injector is mounted inside a high pressure test rig which can take pressures up to 20 atm. The test rig with the LDI injector mounted is shown in Figure 21(b). The pressure vessel has quartz optical windows permitting optical signal acquisition.
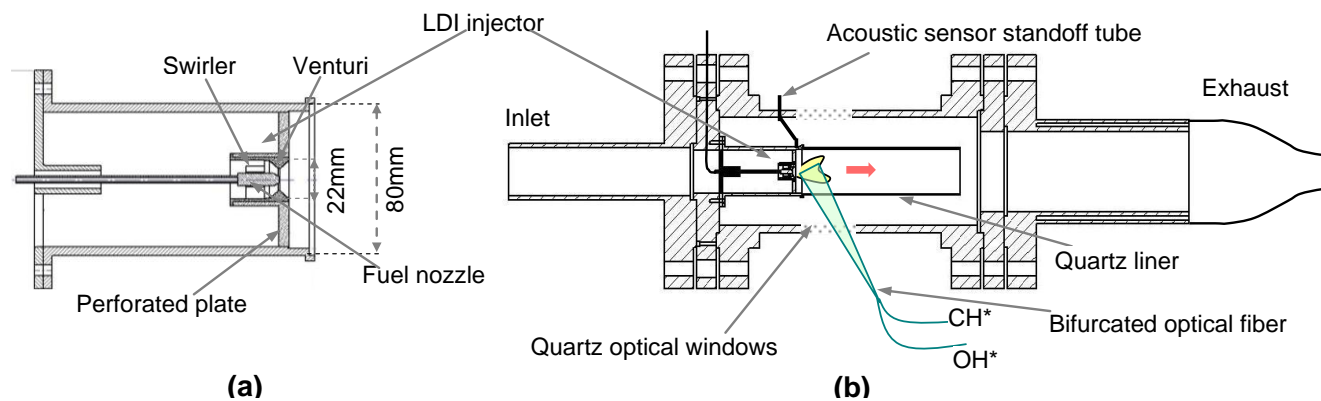

Figure 21. (a) Single element LDI injector (b) LDI combustor in the high pressure test rig.

The average flow velocity (in the absence of combustion) within the combustor (i.e., the quartz tube) is between 9 and 15 m/s and the thermal loading of the combustor is between 28 and 74 kW. A bifurcated optical fiber with a cone angle of 32° is used for collection of optical emissions from the combustor. The fiber is placed nominally at 45° angle to the combustor viewing most of the flame as shown in Figure 21(b). The optical radiation from the collection end of the fiber is split into two parts by the bifurcated fiber: one part passes through an interference filter centered at 308 nm corresponding to OH[*] emission and the other through a 419 nm filter corresponding CH[*] emission. The same type of photomultipliers used in the gas-fueled setup is also used to detect the optical signals here. Acoustic radiation from the flame is

monitored using a Kistler piezo-electric pressure transducer mounted on a standoff tube connected to the combustor.

LDI Combustor development

Since this was the first time this version of the single element LDI combustor has been operated in a co-flow facility, great attention was devoted to ensuring its operation was similar to the expected behavior of an LDI system. Specifically, the single element LDI injector should have a lean partially premixed flame, with low emissions, similar to the full nine-element NASA LDI injector.[44] In addition, similarity in qualitative flame shape and flame size to the multi-element injector is desired, as practical combustors would employ multi-element configurations.

As noted previously, the single element LDI injector uses a co-flow to partially account for the influence of surrounding swirlers that would be present in a multi-element injector design. In order to provide confinement for the swirling flow leaving the central element, a surrounding flow is created by employing a perforated plate. The mass flow rate ratio between the co-flow and the swirling flow determines the effective confinement. In the original nine element LDI injector, the flow split ratio is eight (between surrounding elements and the central element), with an overall square cross section 76.2 mm on each side. For the single element LDI injector, sitting in a test section with a circular cross section and a 76.2 mm nominal diameter, the flow split ratio that would produce the same average axial velocity ratio (in the absence of combustion) between the center element and the surrounding flow drops to 6.3. However, this does not account for any loss of confinement associated with the absence of swirl in the surrounding flow.

A perforated plate with 2.38 mm diameter holes, uniformly distributed across the plate, with an overall blockage of 88% was designed in order to produce the required flow split ratio of 6.3. However, effective area measurements of the injector and perforated plate indicate the actual flow split ratio was closer to 8. Combustion testing of the injector with this plate produced a "clean" blue flame at atmospheric pressure, but an orange flame at elevated pressures (>2 atm), as shown in Figure 22. In the figure, the velocity
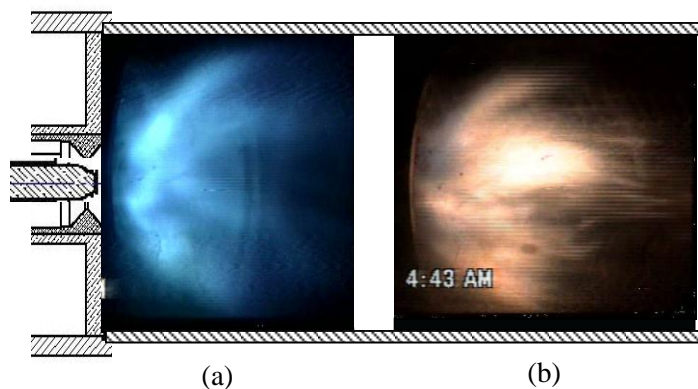

(a)   (b)

Figure 22. Flame in the LDI combustor at (a) 1.17atm, 14m/s, 663K, $\Phi_{overall}$=0.5 (b) 2atm, 10.6m/s, 682K, $\Phi_{overall}$ =0.3.

is the average un-burnt flow velocity and the temperature is the inlet air temperature. Equivalence ratio is the overall equivalence ratio, calculated from using total fuel flow and air flow rates. The existence of a blue flame is an indication of lean premixed/partially premixed operation, whereas the existence of an orange flame indicates formation of soot, typical for non-premixed operation. In addition, the blue flame at ~1 atm can be observed to spread to almost the entire width of the combustor, indicating that the co-flow produced less flame confinement than expected from a multi-element injector, where the flame spread would typically be limited to the size of a single element (25.4 mm). Moreover, the injector produced a twin flame structure, seen

in the blue flame at atmospheric pressure, having two distinctively bright flames. Thus improvements to the injector were required in order to reduce the flame spread and to produce a more premixed (blue) flame at elevated pressures.

In addition to the flow split ratio affecting the flame spread, fuel nozzle tip position relative to the throat of the venturi has also been observed to affect the flame spread significantly. For the images presented in Figure 22, the fuel nozzle tip was located slightly ahead of the venturi throat, by a small distance of ~1 mm. However placing the nozzle tip slightly behind the venturi throat, at a distance of 1.5 mm, produced a significant decrease in flame spread at atmospheric pressure, as shown in Figure 23. In addition, the twin flame structure observed earlier disappeared. Even with this improvement, there was a slight appearance of orange trails in the atmospheric tests, indicating some non-premixedness, and an orange flame was observed at elevated pressures.

Improved operation was obtained by reducing the flow split ratio (close to 6.3). This was achieved by blocking some of the holes in the perforated plate, away from the center. For a given reference velocity, this arrangement results in higher flow velocity surrounding the center and lower farther away. In addition, the fuel nozzle tip was positioned behind the venturi at a distance of ~1 mm. This arrangement produced a blue flame at atmospheric pressure and at elevated pressures, as shown in Figure 24. In addition, the flame spread is reduced, suggesting improved confinement of the fuel/flame by the higher velocity co-flow. All the LBO sensing results in the present paper correspond to the combustor operating in this configuration.
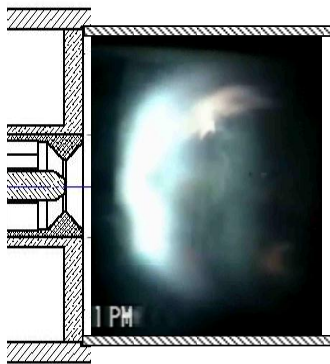

(a)   **(b)**   **(c)**

Figure 23. Flame in the combustor at 1.13 atm, 13.4 m/s, 654 K, $\Phi_{overall}$=0.32, for fuel nozzle position upstream of venturi throat by 1.5 mm.
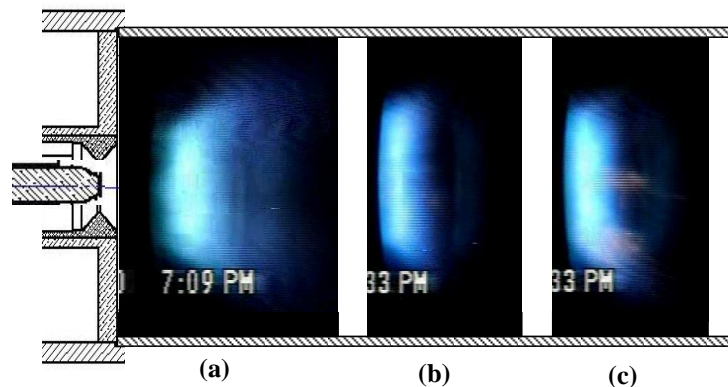
Figure 24. Flame in the combustor at (a) 1 atm, 14 m/s, 663 K , $\Phi_{overall}$=0.41; (b) 2 atm, 10.6 m/s, 682 K, $\Phi_{overall}$=0.28; (c) 4 atm, 12 m/s, 733 K, $\Phi_{overall}$=0.23.

III.D.2 LBO Margin Sensing in the Gas-Fueled Combustor

In the gas fueled combustor LBO margin sensing under dynamically unstable conditions is investigated. Specifically, margin sensing under dynamic instability with two instability mechanisms i.e., instability without equivalence ratio oscillations (w/o Φ') and with equivalence ratio oscillations (w/ Φ') is studied. More details of the margin sensing results are presented in 2nd and 3rd annual reports. A summary of the results are discussed here.

The combustor exhibits pronounced combustion dynamics in lean conditions, over a wide range of equivalence ratios, including very close to blowout, for both kinds of instability mechanisms, with (w/ Φ') and without (w/o Φ') equivalence ratio oscillations. Acoustic signal time traces for both kinds of instability mechanisms and associated power spectra are shown in Figure 25(a) and (b) respectively, for combustor operation near LBO. For the two instability mechanisms all operating conditions are identical, except for the change in fuel injection location. From the power spectra, the combustion instability is evident from the presence of clear peaks at 265 Hz for instability w/o Φ', and 245 Hz for instability w/ Φ'. These frequencies are close to the quarter wave mode of the combustor. A clear difference between the two types of dynamics is the presence of strong amplitude modulations for instability w/ Φ', absent in the instability w/o Φ', seen in the time traces of Figure 25(a). The amplitude modulations result in broader range of frequencies observed in the power spectrum (Figure 25 (b)) for instability w/ Φ'. Disparities in the behavior of dynamics are an indication that the instability mechanisms are different, as desired.

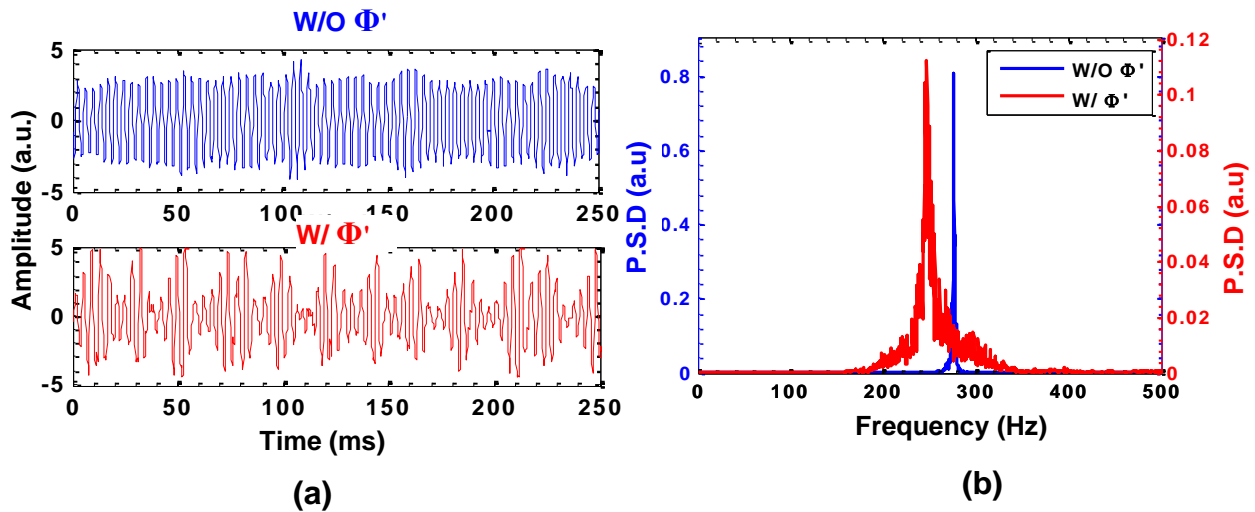**(a)**   **(b)**

Figure 25. (a) Acoustic signal time traces for combustor operation near LBO (Φ-Φ_{LBO}=0.03), for instability w/ and w/o Φ'. (b) Corresponding power spectra.

Optical signal time traces for combustor operation near LBO, for both kinds of instabilities, are shown in Figure 26. For instability w/o Φ' there are large amplitude modulations, and the amplitude minima are well above zero, except for t=100-150 ms. At this instance, there is little modulation and the amplitude drops close to zero. The signal behavior during this instance is similar to that observed for precursor events in dynamically stable conditions, where the local signal amplitude goes to zero during precursors due to flame extinctions. Such signal features were
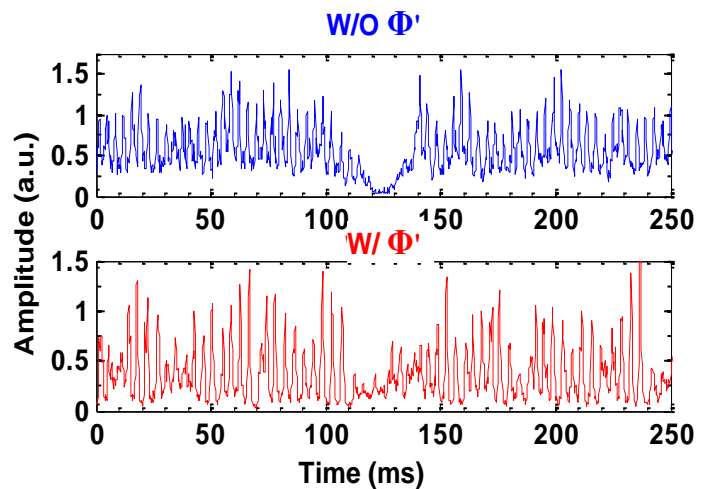

Figure 26. Optical signals with precursor events (~ 100-150 ms) for dynamics w/o Φ' and w/ Φ'.

observed only close to LBO, indicating that this is a LBO precursor. Unlike dynamics w/o Φ', those w/ Φ' have amplitudes dropping to zero during each instability cycle, and this behavior is not restricted to near LBO conditions; thus the low amplitudes alone cannot be taken as indication of proximity to LBO. However there are other instances in the signal which may be precursor events. For example at 100 ms there are no amplitude modulations and the local signal mean stays well below the normal mean value, similar to a precursor event. Such events are observed only close to LBO, indicating that they are precursors. Both events have similar durations of about 35 ms. As the two events look qualitatively different, they would require different thresholding approaches for detection. For example, for dynamics w/o Φ', the precursor can be identified with a double thresholding method, with thresholds set as μ-$\kappa\sigma$. However, the same cannot be used for instability w/ Φ', as during precursors signal amplitude does not go below the nominal signal minima.
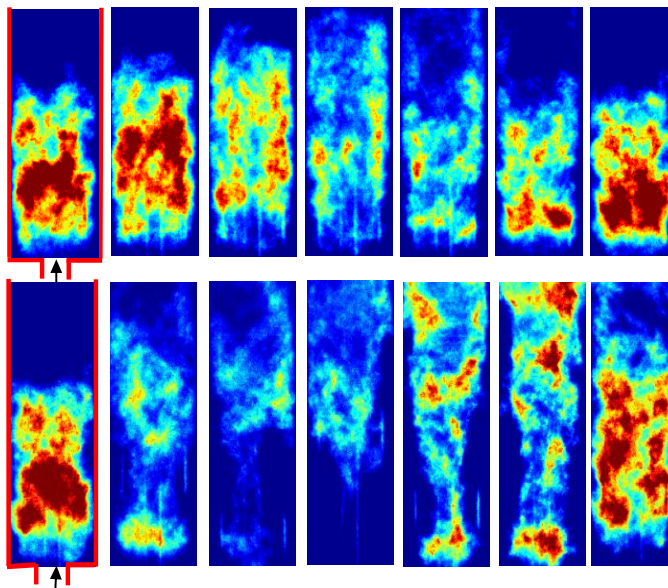

Figure 27. High speed flame images for instability w/o Φ' (top) during an instability cycle; image separation 0.58ms (bottom) during a precursor event; image separation:6.8ms.

High speed flame images during normal combustor operation and during a precursor event similar to the one above, for combustor operation near LBO having instability w/o Φ' are shown in Figure 27. Normal combustor operation is characterized by instability cycles, and from the high speed images flame length and intensity modulations over a cycle can be observed. Combustor operation far from LBO has similar periodic instability cycles. During a precursor event flame extinction around the inner recirculation zone, followed by its recovery, can be seen. During this period of extinction flame switches to a lifted configuration, with most of the burning occurring downstream. The stable flame around the inner recirculation zone and the temporarily lifted flame can be considered two different flame modes. Precursor events in this combustor are associated with flame switching between these two modes. Such flame behavior is consistent with observations in dynamically stable conditions.

Similar high-speed flame images for typical combustor operation for instability w/Φ' are shown in Figure 28 (a), along with a simultaneous optical signal trace in Figure 28(b). In the images, a region of about 2.5 cm in height at the inlet of the combustor is not optically accessible, unlike the images shown in Figure 27. In contrast to the instability w/o Φ', normal combustor operation for instability w/ Φ' is characterized by unsteady instability cycles, i.e., regular growth and decay in instability amplitude, as can be seen in Figure 28 (b). From the 2nd and 3rd high-speed images, during troughs of an instability cycle, some amount of flame extinction is observed. Though partial extinction is occurring during these instability cycles, they should not be considered LBO precursors as the combustor shows no tendency to lose

combustion on an average sense in this operating range. Such statically stable operation could result from the instability amplitude decaying after its initial growth, thus leading to more stable flame as seen in the last two frames. If the instability amplitude were continue to remain the same, or even rise, it might lead to complete flame loss and blowout.
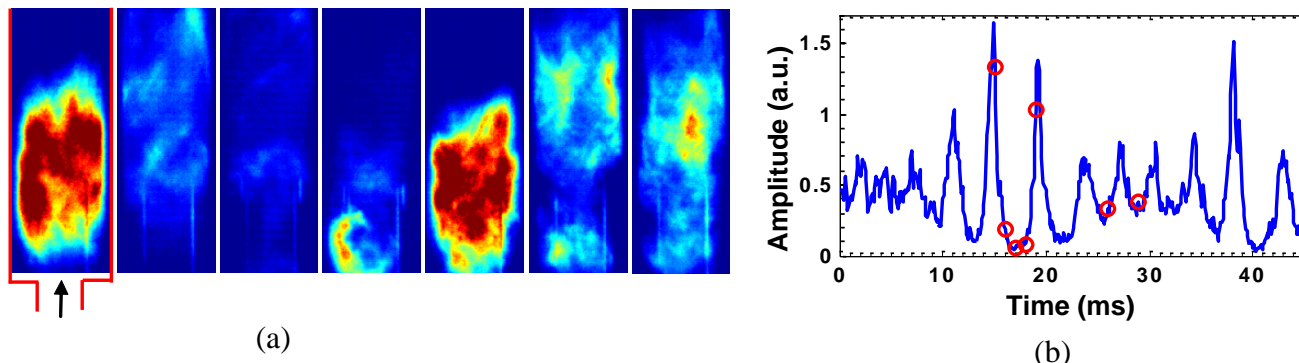

(a)   (b)

Figure 28. (a) High speed flame images (b) simultaneous optical signal time trace for instability w/ Φ' during normal combustor operation.

In contrast to the short duration extinctions shown above, Figure 29 contains a sequence of high-speed flame images with extinction occurring for a much longer duration (~23 ms) and with more pronounced extinction for instability w/ Φ'. Such long duration extinctions were found to occur only near LBO, and hence can be considered precursors. Flame behavior during the extinction is similar to instability w/o Φ'.

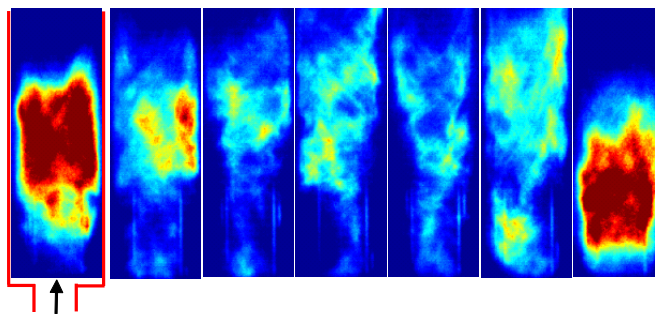Figure 29. High-speed flame images during a precursor event for instability w/ Φ'. Image separation 6ms.

In addition to optical emissions, acoustic emissions can be used for monitoring LBO precursor events as acoustic radiation is proportional to the time derivative of heat release rate. Acoustic signals from the combustor acquired simultaneously with the optical signals are presented in Figure 30. For instability w/o Φ', dynamic instability amplitude reduction is observed during the precursor. However, for instability w/ Φ' no such distinct amplitude reduction is observed during the precursors; rather only the significant amplitude modulation (breathing) is seen. Dynamic instability amplitude
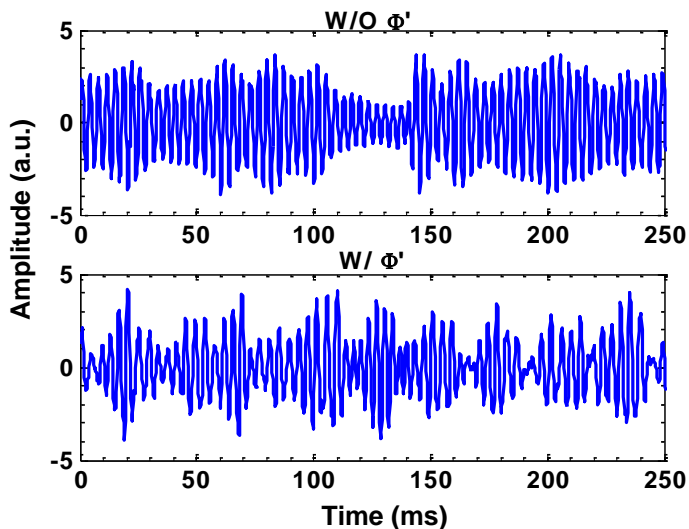

Figure 30. Acoustic signals during precursor events, with precursors identified from the simultaneously acquired optical signals (

Figure 26).

32

reduction cannot be considered as a precursor event as it is primarily dependent on acoustic-heat release coupling process, and is not uniquely attributable to the occurrence of extinction events. Therefore, precursors are not clearly evident in the raw acoustic signals in the presence of combustion dynamics.

From precursors in the optical signals, the duration of the extinction and re-ignition process is about 35 ms. Therefore in the acoustic signals, features corresponding to precursors should have similar time scales. On the other hand, dynamic instability period is about 4 ms for both instabilities, much shorter than the precursor event time scale. Therefore, signal processing techniques such as low pass filtering can be employed for suppressing dynamic instability component and expecting to improve precursor event detection. The acoustic signal time trace for dynamics w/o Φ' was low pass filtered at 100 Hz using an 8th order digital Butterworth filter. The result is shown in Figure 31. In the filtered signal, the precursor signature is clearly evident. In the un-filtered signal the precursor is shadowed by existence of high amplitude dynamic instability. A similar precursor signature becomes evident for dynamics w/ Φ' after low pass filtering (not shown). Thus, low-pass filtering is a demonstrated approach that can be employed for precursor event detection from acoustic signals in the presence of combustion dynamics.
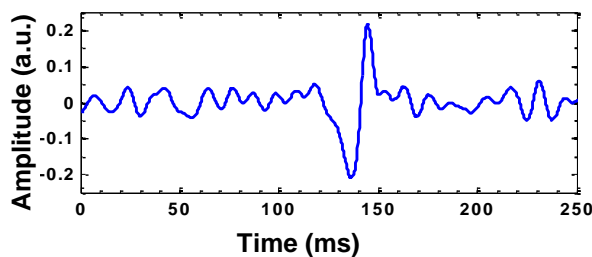

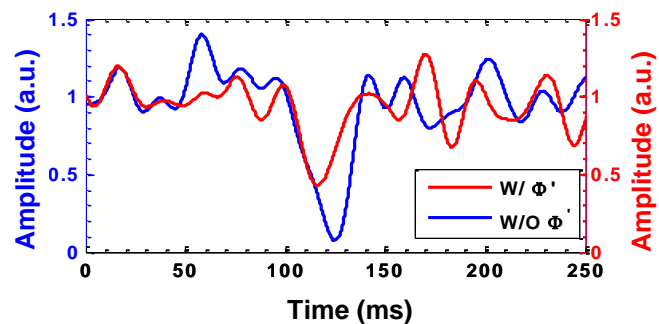Figure 31. Low-pass filtered acoustic signal with a precursor event.

Figure 32. Low-pass filtered optical signals with precursor events.

Employing the same low-pass filtering approach (at 50 Hz) to the optical signals results in similar precursor signatures for both kinds of instabilities, as shown in Figure 32. In addition, using low pass filtering even for dynamically stable conditions suppresses the combustion noise and results in a similar event signature to that seen with dynamics. Thus applying low-pass filtering for optical signals provides the ability to use a single sensing algorithm, regardless of the state of dynamic instability in a combustor, i.e., dynamically stable or unstable without regard to the instability mechanism. In summary, signal filtering at an appropriate frequency shows promise for robust precursor event detection.

As in previous works, the average event occurrence rate can be shown to be an indicator of proximity to LBO. The event occurrence rate, averaged over a 30 second duration, obtained from low-pass filtered optical signals at 50 Hz, is shown in Figure 33. As expected, the event occurrence rate increases near the combustor's LBO limit. In addition, instability w/ Φ' has slightly higher event rate compared to instability w/o Φ'. Besides event occurrence rate, analysis of the current results indicates that other event features can change as LBO is approached. Specifically, the duration of an event and the modulation depth below the mean are observed to

increase near LBO as well. Combining all these, a more robust LBO proximity parameter, the Stability Index (*SI*), is proposed. *SI* essentially integrates the signal loss below the mean during precursor events and is given in Eq. (34). Event occurrence rate and *SI*, normalized with their corresponding average values far from LBO (Φ-Φ_{LBO}>0.04), for instability w/o Φ', are plotted in Figure 34. From the figure, *SI* provides a higher dynamic range compared to the average event occurrence rate.

$$SI = \frac{\sum\limits_{i=window} \left(\bar{C} - C_i\right)\Delta t_i \delta_{event}}{\bar{C}\Delta t_{window}} \qquad (34)$$
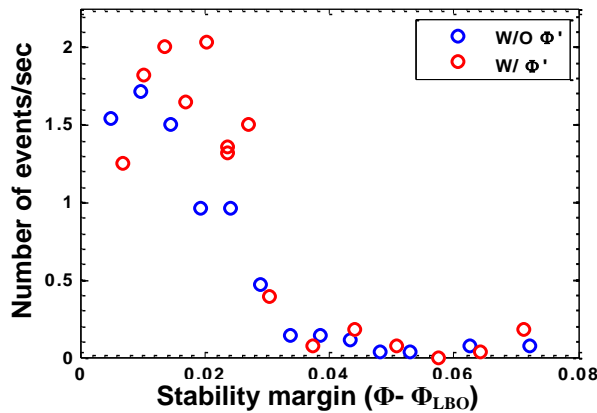

Figure 33. Average event occurrence rate for both kinds of instabilities obtained from optical signals.
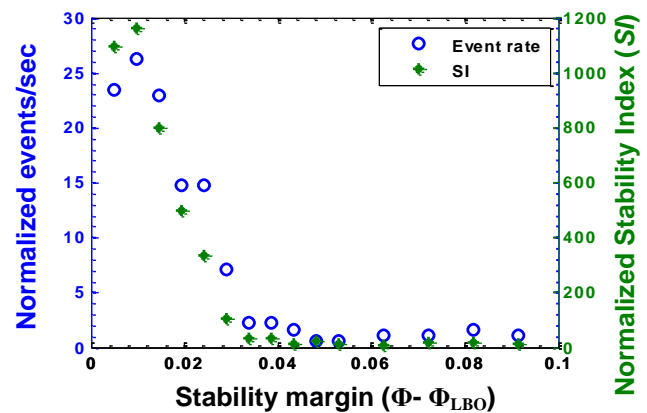
Figure 34. Average event rate and SI in normalized form for instability w/o Φ' obtained from optical signals.

Event durations for instability w/o and w/ Φ' are shown in Figure 35. The durations are obtained from un-filtered optical signals and defined as time spent by the signal below the mean during an event. From the figure it can be seen that instability w/ Φ' has clearly lower event durations compared to events w/o Φ'. The disparity in event rate and duration might be resulting from the effect of instability on the extinction and re-ignition process. It can be speculated that low equivalence ratios during equivalence ratio oscillation cycles could be increasing the propensity of flame to extinction, resulting in more events. In addition, equivalence ratio oscillation cycles could be creating regions of high equivalence ratio, promoting re-ignition of the flame and thus lowering event durations.

Average event rates for both instability mechanisms obtained from low-pass filtered acoustic signals are plotted in Figure 36. Similar to events from optical signals, events in acoustic signals increase near LBO. Events for instabilities w/o Φ' provide a good measure of LBO approach, with a monotonic increasing trend. On the other hand, for instabilities w/ Φ' the number of events varies non-monotonically and produces a lower occurrence rate near LBO compared to the w/o Φ' case. The reason for such performance could be due to not all the events being detected. This could arise from sharp drops in heat release for instability w/ Φ' during precursor starting, producing high frequency signal content in the acoustic signals that are suppressed by low-pass

filtering. In addition amplitude modulations give rise to increased noise even in the filtered signals making it harder to detect events.
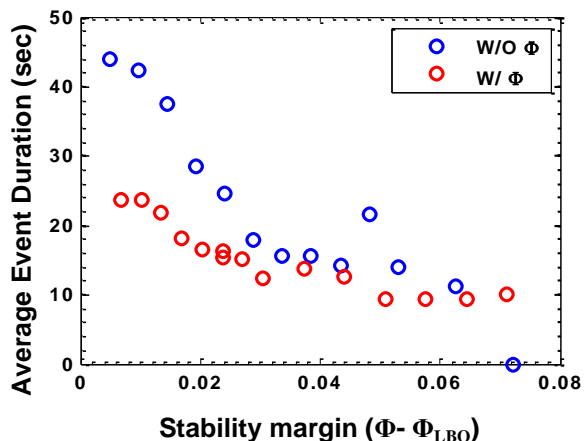

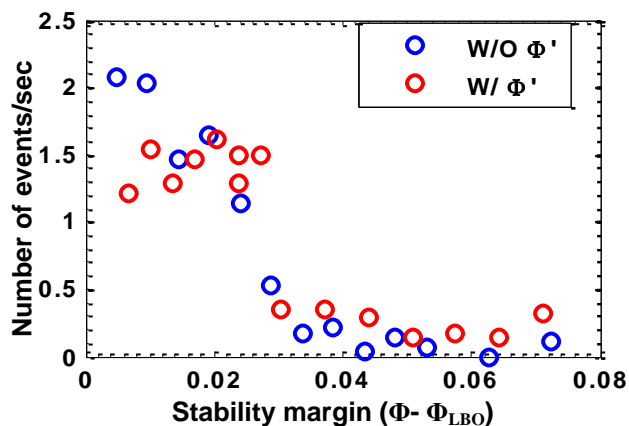Figure 35. Average event durations for both kinds of instabilities.

Figure 36. Average event rates from acoustic signals for the two kinds of instabilities.
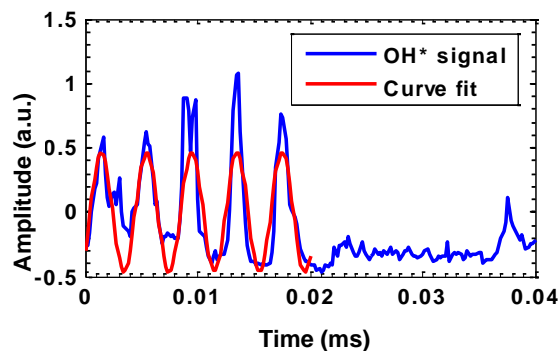

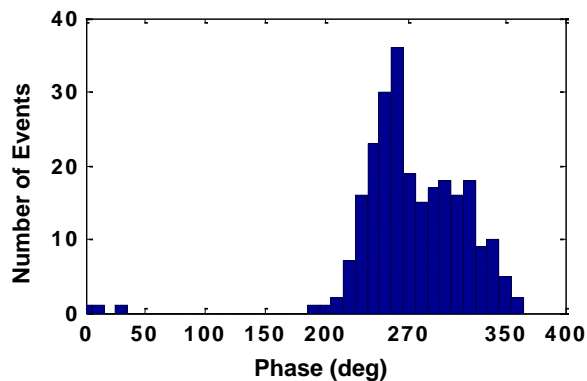Figure 37. Optical signal instability cycles before starting of a precursor fitted with a *sine* function.

Figure 38. Histogram of instability cycle phases at staring of precursor events.

For combustion not having dynamic instability, precursor events can be expected to be triggered by small random disturbances. However, in the presence of combustion dynamics equivalence ratio oscillations and velocity oscillations can be expected to trigger events. From optical signal data for instability w/ Φ' it has been observed that precursors are usually starting at troughs of instability cycle. To obtain the instability phase at the starting of precursors, optical signal data 20 ms prior to precursors is fitted with a harmonic *sine* function as shown in Figure 37. The *sine* function is $A\sin(2\pi f t + \alpha)$ where *f* is instability frequency and α is phase. The process is repeated for 248 events to get a histogram for the phase and is shown in Figure 38. As evidenced in the histogram, most of the events occur near a phase of 270º, corresponding to the troughs of instability cycles. The width of the histogram can be attributed to errors in obtaining the phase

while curve fitting. Assuming most of the heat release oscillations (OH* signal amplitude) is caused by equivalence ratio oscillations, instability troughs correspond to troughs in equivalence ratio oscillation cycles. The result indicates that most of the time, precursors are triggered by equivalence ratio oscillations. The same process could not be performed for instability w/o Φ' as extinction is more gradual (see

Figure 26) and the precise time when events start could not be determined.

III.D.3   LBO Margin Sensing in the LDI Combustor

The following LBO margin sensing results in the LDI combustor correspond to operation at 2 atm and about 700 K inlet air temperature.

The LDI combustor exhibits a moderate level of dynamic instability. This is evidenced by the peaks in the power spectra of the optical (CH*) and acoustic signals, which were recorded near the combustor's LBO limit (see Figure 39). The acoustic power spectrum illustrates the complexity of the dynamics, as there are multiple local peaks in the spectrum. For example at this 2 atm condition, there are multiple modes (peaks) at approximately 580, 660 and 725 Hz, as well as their harmonics. The strongest mode at 660 Hz corresponds to the axial quarter wave mode of the combustor, based on an assumed uniform gas temperature of ~1700 K. It has a sound pressure level of nearly 120 dB. In the optical power spectrum, the power is distributed over a similar broad range of frequencies, with a lower fraction of the power at the

Figure 39. Power spectra of optical and acoustic signals for LDI combustor operation near LBO.

instability frequencies. For more pronounced combustion dynamics, nearly all the power would be expected to be in narrow ranges around the instability frequencies. While only 2 atm results are shown here, 4 atm operation produces a similar behavior.
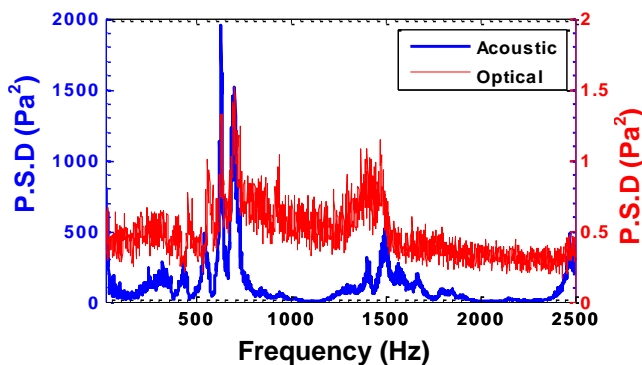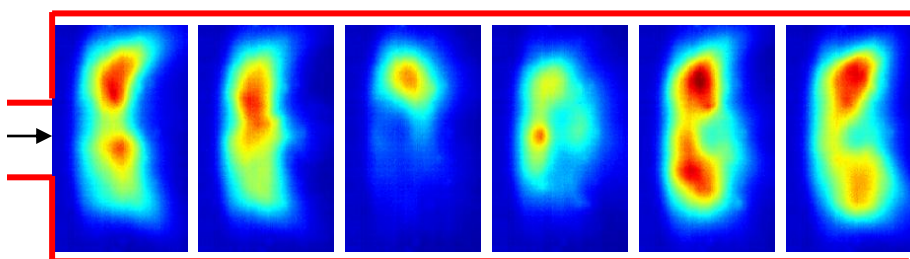

Figure 40. High speed flame images during a precursor event in the LDI combustor.

The LDI combustor flame clearly exhibits temporary partial flame extinctions near LBO, as evident in the high-speed flame images shown in Figure 40. The images are acquired by successive 1 ms camera exposures, with the camera viewing at an angle of 45° from downstream direction, similar to the optical fiber, shown in Figure 21. The images in the 3rd and 4th frames show a signification amount of flame extinction, followed by its recovery in subsequent frames.

Far from LBO, no such extinctions are observed and the flame appearance is similar to that of the flame in first two or the last two frames, with some unsteadiness. From observations of the high speed images during other extinction events, there is no single, preferable region where extinction occurs. From the images, duration of the extinction is approximately 2-3 ms, as some of the extinction could be present in 2nd and 5th frames as well. These durations are much shorter than the durations in the gas-fueled combustor (20-50 ms). Presumably, the extinctions are caused by the existence of lean conditions and high turbulence levels in the shear layer between the inner recirculation zone and the surrounding flow, where the flame is expected to exist. After extinction, re-ignition may be accomplished by hot products/radicals still present in the recirculation zone or flame propagation into reactants in the extinct regions of this swirling flow.

An optical signal time trace, near LBO with precursor event like features (indicated by arrows) is shown in Figure 41 (top image). The signal features are characterized by temporarily low amplitude, for an extended duration, compared to the neighboring region, typical for LBO precursors. Flame extinction images shown Figure 40 correspond to such events in the optical signal. Signatures of such precursor events are much smaller than the ones observed in the gas fueled combustor, where precursors standout more clearly. The duration of the precursor events is in the range 1.5-3 ms. The short duration time scales are similar to the dynamic instability period (1.4-1.7 ms) in this combustor. Low-pass filtering at 500 Hz, corresponding to a 2 ms time period, has been observed to suppress instability and other high frequency noise thus improving event signatures. The low-pass filtered optical signal, with precursor events standing out more clearly, is shown in Figure 41(bottom). The duration of precursors in the LDI combustor is much shorter than the gas fueled combustor (20-50 ms). Similarly short duration precursors (~6 ms) were observed in prior LBO sensing studies in a conventional (non-LDI) liquid fueled combustor.[45]
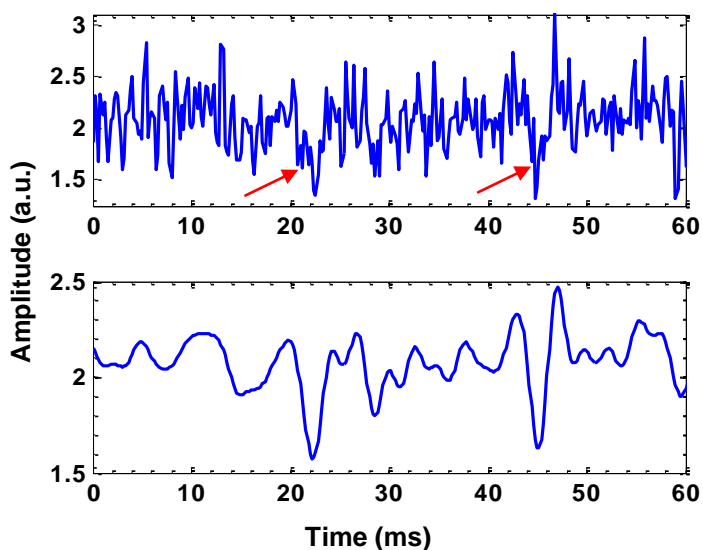

Figure 41. Optical signal time trace with precursor events in the LDI combustor (top) un-filtered (bottom) low pass filtered at 500Hz.

LBO precursor events in the filtered optical signals can be detected using a double threshold approach. An event starts when the signal drops below a first threshold and ends when the signal rises above a second higher threshold. Such a detected event is only considered valid if it exhibits a minimum required duration (time between the two threshold crossings). Thus the event detection includes a minimum required modulation depth and a measure of event duration.

Results of precursor event identification, based on signal recordings of 40 sec duration for each equivalence ratio, obtained from low-pass filtered CH^{*} signals, are displayed in Figure 42. The threshold settings are: a lower threshold of μ-3.25σ, an upper threshold of μ-0.5σ, and a minimum duration of 1.6 ms. The threshold settings are optimized to produce a low event rate far from LBO and maximum possible near LBO. The filtered signals require a slightly lower upper

threshold (μ-0.5σ) than the mean (μ), as the signal can spend a long time just below the mean, before crossing it, artificially increasing the event duration. This is primarily a result of applying low pass filtering. From the figure, event occurrence rate stays near zero far from LBO and increases monotonically as the stability margin is reduced. The event rates near LBO are much higher compared to the gas fueled combustor (1-2/sec). Events start to occur around Φ/Φ_{LBO}=1.25, more clearly seen in the expanded inset plot with the vertical scale reduced.
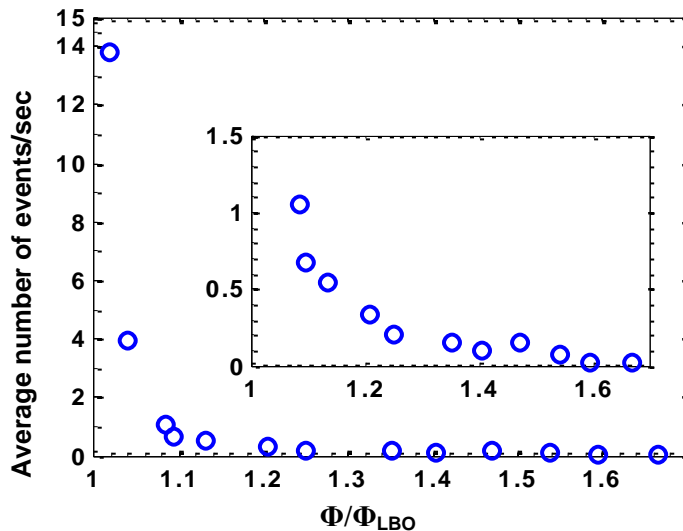

Figure 42. Average event occurrence rate from low pass filtered CH^* signals.

Though precursor event occurrence rate provides a satisfactory LBO proximity parameter, it is important to examine its sensitivity to the threshold settings. For robust detection, small changes in the threshold settings should not produce significantly different results. The sensitivity of the event identification approach to the threshold settings is examined by perturbing the baseline settings: lower threshold μ-3.25σ, upper threshold μ-0.5σ, and minimum duration constraint 1.6 ms. The perturbation to the lower threshold limit is examined in Figure 43, where the baseline threshold (μ-3.25σ,) varied by $\pm$0.25σ. The event occurrence rate trend does not change significantly, though changing the lower threshold setting slightly changes the average event occurrence rate. Figure 44 shows the sensitivity to the minimum event duration constraint, with the baseline setting (1.6 ms) perturbed by $\pm$0.2 ms. Again, the overall trend is the same for all the cases, with small changes again in the occurrence rate.
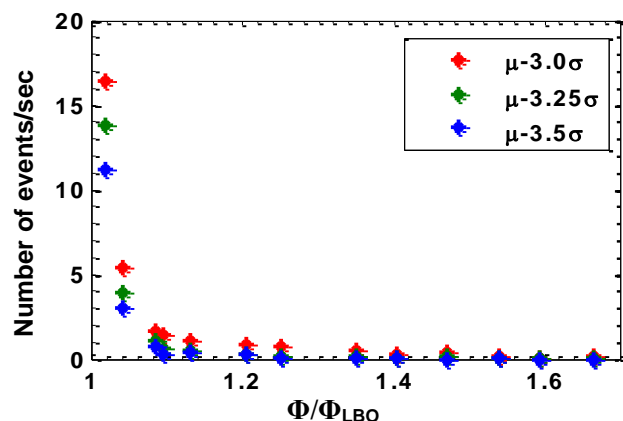

Figure 43. Average event rate for different lower threshold settings; upper threshold: μ-0.5σ, and 1.6 ms time constraint.
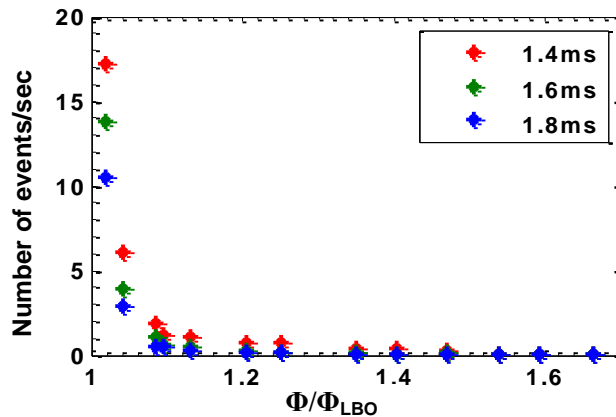

Figure 44. Average event rate for different time constraints, with lower threshold μ-3.25σ, upper threshold μ-0.5σ.

The above results were presented for event detection using CH^* chemiluminescence; OH^* signal is an alternative as both are generally proportional to heat release rate. Precursor events

detected in low-pass filtered CH[*] and OH[*] signals with optimized threshold settings to produce a low event rate far from LBO and high event rate near LBO are compared in Figure 45. Both optical signals were acquired simultaneously with the same optical fiber probe, with the light exiting the probe split and sent to two spectrally filtered detectors, one for CH[*] and the other for OH[*]. The optimized lower threshold for OH[*] ended up farther from the mean (μ-4σ) than CH[*](μ-3.25σ). Using the CH[*] threshold value, the OH[*] signal produced too high an event rate (~1/sec) far from LBO. However, it produced similar event rates near LBO. Even with the separately optimized thresholds, the OH[*] sensing results in lower event rates near LBO. This indicates some differences in the background CH[*] and OH[*] emissions far from LBO.

Normalized unfiltered and low-pass filtered CH[*] and OH[*] signals, during a precursor detected in the filtered OH[*] signal at Φ/Φ_{LBO}=1.54, are plotted in Figure 46. In the filtered OH[*] data, the feature indicated by the arrow is detected as a precursor, since it has a relatively large modulation depth compared to the nominal signal. However in the corresponding filtered CH[*] signal, the modulation depth is considerably lower and hence not detected as an event. Examining the unfiltered signals during this period, OH[*] has a slightly higher modulation depth and duration compared to CH[*] (1.2 ms for OH[*] and 0.8 ms for CH[*]). Though the unfiltered signals have a slight difference in modulation depth, the difference is more pronounced in the filtered signals. The filtering suppresses the CH[*] feature more as it has a shorter time scale. The difference in modulation depths for OH[*] and CH[*] are not surprising, as the two respond somewhat differently to variations in heat release and unsteady combustion processes. For example, CH[*] and OH[*] emission respond differently to perturbations in local equivalence ratio and strain. Since CH[*] signals provide a better LBO proximity parameter in the present study, they are used in the remaining results.
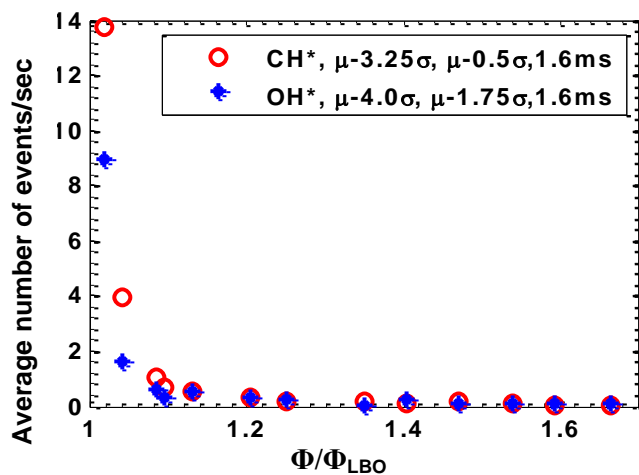

Figure 45. Average event rate from low pass filtered CH[*] and OH[*] signals with different threshold settings.
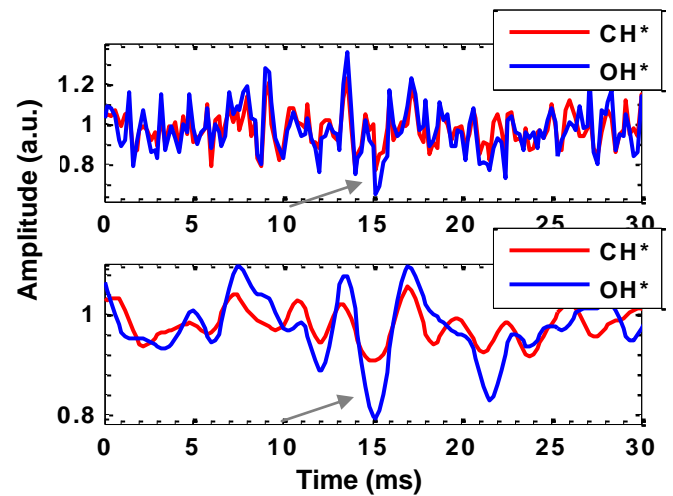
Figure 46. CH[*] and OH[*] signals during a precursor detected in filtered OH[*] signal; (top) unfiltered (bottom) filtered signals. (Φ/Φ_{LBO}=1.54).

Besides event occurrence rate increasing near LBO, modulation depth of an event and its duration can be expected to increase as stronger extinctions for a larger time are likely to occur near LBO. Average modulation depth of an event, normalized by the local signal mean, and

average duration (duration below μ-0.5σ limit) obtained from filtered CH* signals, using μ-3.25σ, μ-0.5σ thresholds with a time constraint of 1.6 ms for event detection, are plotted in Figure 47. The stability margin range above Φ/Φ_{LBO}=1.7 is omitted, as very few events occur in this range and likely represent noise. As seen in the figure, both event duration and modulation depth generally increase as the stability margin is reduced. Therefore combining event duration and modulation depth with event occurrence rate, using the Stability Index (*SI*) should provide a more robust LBO proximity parameter.

The Stability Index and event occurrence rate, normalized with the corresponding average values far from LBO (Φ/Φ_{LBO} =1.25-1.7), are plotted in Figure 48. *SI* is calculated by integrating signal loss below a μ-0.5σ limit during precursor events. From the figure, *SI* provides a higher dynamic range compared to the average event occurrence rate. However, there is no appreciable improvement in early warning margin.
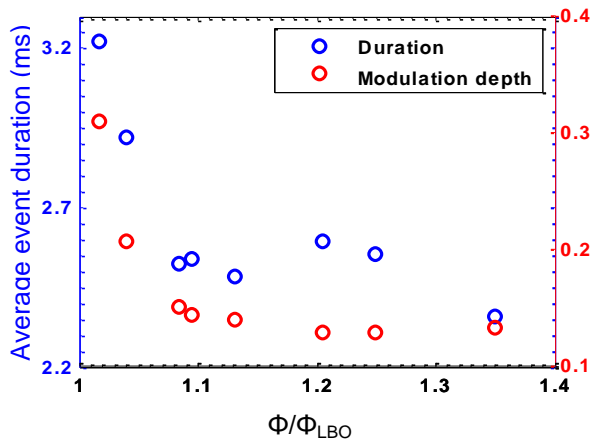

Figure 47. Average duration of an event, below the μ-0.5σ limit and average maximum modulation depth of an event, obtained from filtered CH* signals.

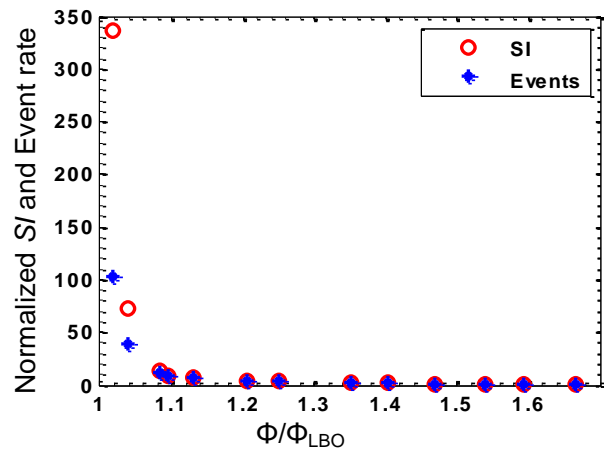Figure 48. *SI* and event rate, normalized with corresponding far from LBO(Φ/Φ_{LBO} >1.25) values, obtained from filtered CH* signals.

The potential for real time LBO proximity sensing using precursor events is examined in Figure 49. Here, the fuel flow rate is continuously decreased starting from t=30 sec until LBO occurs at t=93 sec. The event occurrence rate and *SI* at a time t are obtained by considering a one second interval from t-1 sec to t, using the low pass filtered CH* signal acquired simultaneously with the fuel flow rate signal. Far from LBO, no events are detected. Events clearly start to appear at Φ/Φ_{LBO}=1.3 (t=60 sec). The event occurrence rate appears to vary widely at this point, ranging from 1 sec^{-1} to 5 sec^{-1} between Φ/Φ_{LBO}=1.3 and 1.1 (i.e., t=60-68 sec). It then rises sharply at Φ/Φ_{LBO}=1.1. The *SI* provides a smoother, less noisy trend near LBO, compared to the basic average event occurrence rate.
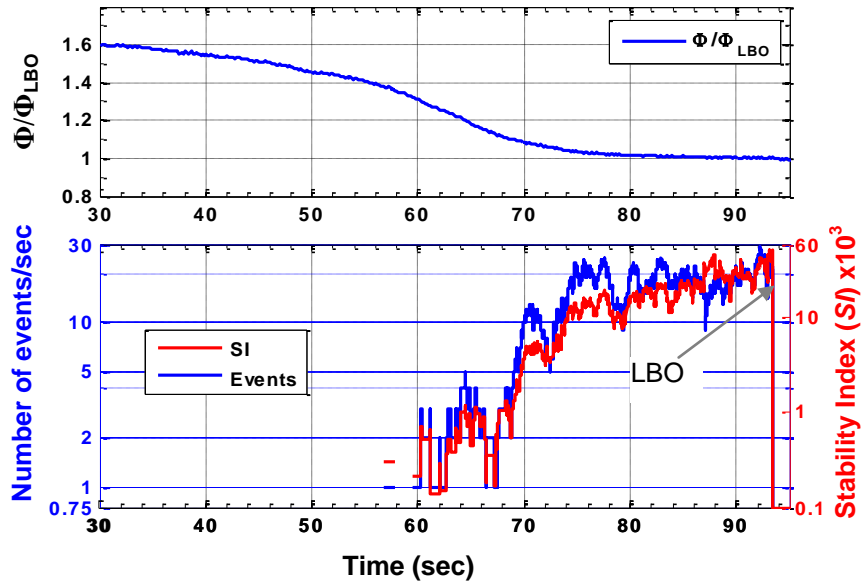
Figure 49. (top) Stability margin variation with time (bottom) Number of events and SI calculated in 1sec, in real time.

Event detection using acoustic signals was also investigated. Since the optical and acoustic signals were recorded simultaneously, the acoustic signal could be examined during times that the optical signal showed a precursor event. The acoustic events should be slightly delayed due to the propagation time between the flame and transducer, about 2 ms in the LDI rig. Examining times corresponding to prominent optical events we found some indication of a precursor, but the character of the acoustic signal during the event was not distinct from other times. Low pass filtering the acoustic signal at 500 Hz did little to improve the situation. Therefore, robust precursor event detection was not achieved with the acoustic sensing, as precursors could not be identified without also detecting numerous spurious events.

There are a number of possible reasons for the absence of a clear precursor event signature in the acoustic signal. For one, the presence of dynamic instabilities makes it harder to detect precursor events, as observed earlier for LBO sensing during strong combustion dynamics in the gas-fueled combustor. The shorter duration of the precursors in the LDI system makes this even more difficult. When the duration of precursor events and the dynamic instability periods are sufficiently different, filtering is able to separate precursors from dynamics. However as the time scales of both get closer, acoustic precursor event detection is preferentially compromised. This can be explained by analyzing the amplitude spectral content of the signals.

Combustion dynamics produce periodic oscillations in heat release and pressure having harmonic nature. The signals have spectra that are narrowband, having peaks at instability frequencies. However, amplitude variations and phase drifts could result in some broadening in instability spectra. In addition, higher harmonics or different modes would result in multiple peaks in the spectrum. Precursor events are discrete, intermittent, and typically occur at a slow rate (e.g., 10-20 events/sec). For a discrete precursor, the spectrum is broader as it is essentially the convolution of the spectrum of a periodic precursor with the spectrum of a boxcar truncation function with a width given by the duration of the precursor. This is similar to spectral

broadening caused by using a finite signal for spectrum evaluation. Model optical and acoustic precursor event time traces, along with their amplitude spectra are plotted in Figure 50. In the figure, the time axis of the precursor events is normalized by the duration of the precursor events, giving a unit time scale for the events. Similarly in the spectra, frequency is normalized by the duration of the precursors; unit frequency corresponds to the inverse of the precursor time scale.

As seen in the amplitude spectra, both optical and acoustic precursor signals have quite wide spectra. For a dynamic instability having the same period as the precursor duration, the spectrum would be narrow and at unit frequency. This fact implies that even if durations of precursors and instability are similar, filtering (lowpass or a narrow bandpass around the instability frequency) would still be effective in improving precursor signatures. Acoustic precursors have a relatively higher amount of power above unit frequency compared to the optical signal. Hence, lowpass filtering would suppress acoustic precursors more than optical precursors.
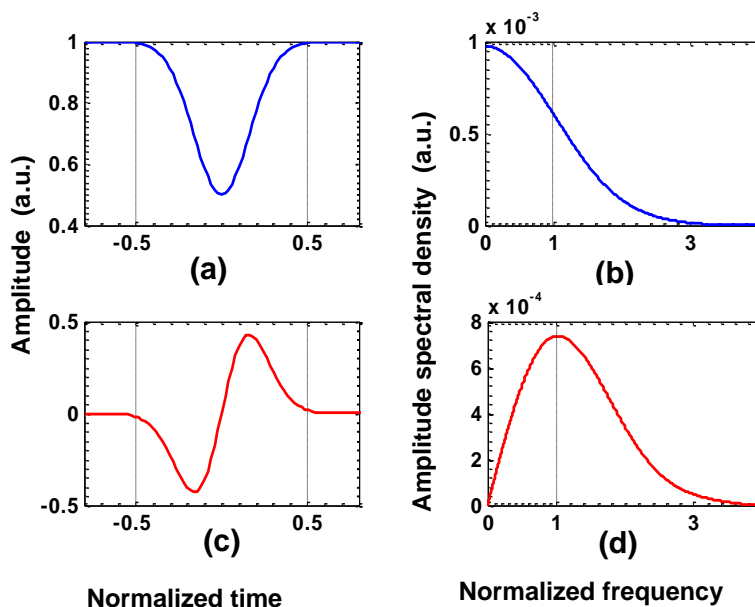

Figure 50. Precursor events and their spectral content; (a) optical precursor (b) its amplitude spectrum (c) acoustic precursor (d) its amplitude spectrum.

There is another, more important reason that acoustic sensing in a confined combustor would be less robust than optical sensing. The acoustic pressure measured by the pressure transducer, at a given time, is not solely from acoustic emission at a single instant. It has components of acoustic emission from a range of previous times, reflected from boundaries, which could contribute to "noise" in the acoustic signal, making it harder to detect precursors. This is not the case for optical sensing.

To examine the impact of reflections on detection of acoustic precursors, a simple combustor model as shown in Figure 51 was developed. The model consists of two regions with different impedances separated by a thin flame. The pressure transducer is assumed to be mounted near the inlet of the combustor on the wall. An acoustic precursor is assumed to be created at the flame and travels to the left and right sides. It gets reflected from the inlet, the flame and from the end wall. Acoustic impedance in each region is given by $Z = \rho C$. Reflection and

transmission coefficients for a pulse traveling from region 1 to 2 are given by Eq. (35) and Eq. (36) respectively. The inlet is assumed to be perfectly reflecting with $Z_0 = \infty$. Impedance of the end wall (Z_L) is given by Eq. (37) taking into account end wall effects and mean flow. Other required parameters are assumed to mimic the LDI combustor: distance from the inlet to the flame, $L_1 = 3$ cm and flame to the end wall, $L_2 = 27$ cm; $T_1 = 700$ K; $T_2 = 1970$ K; and P=2 atm. The acoustic precursor is assumed to have a shape as shown in Figure 50 having a duration of 2 ms generated at time=0.

$$R_1 = \frac{Z_2 - Z_1}{Z_2 + Z_1} \tag{35}$$

$$Tr_1 = \frac{2Z_2}{Z_2 + Z_1} \tag{36}$$

$$Z_L = \rho C \left(\left(\frac{k^2 a^2}{4} - i0.613ka \right) + M_L \right) \tag{37}$$
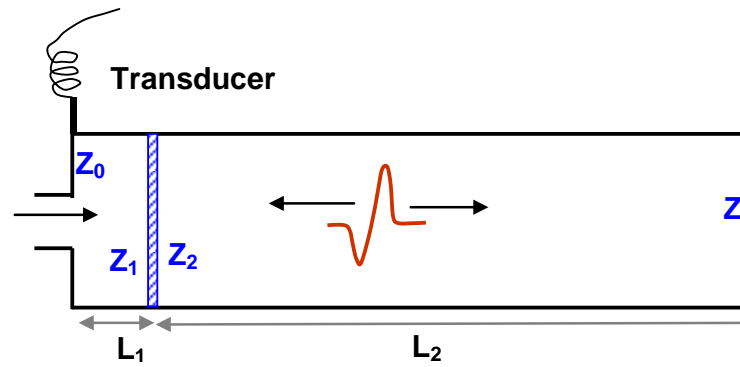

Figure 51. Combustor model for acoustic precursor reflections modeling.

Each time a precursor pulse goes through the flame, it creates two pulses, one reflected the other transmitted. This gives rise to numerous pulses crisscrossing inside the combustor. Pulses are dissipated at the end wall due to the end wall reflection coefficient being less than one. The final pulse measured by the transducer is a superposition of multiple pulses separated by different delay times. The final pulse along with the actual pulse is shown in Figure 52. Unlike a single precursor the reflected precursor is ringing in nature with few cycles. Amplitude spectra of the two precursors are shown in Figure 53. The spectrum of the reflected precursor is close to the natural frequency of the combustor which is usually the combustion dynamics frequency. This manifestation makes it hard to separate the precursor from dynamic instability.

To demonstrate the effect of difficulty in separating the reflected precursor from combustion dynamics, a reflected precursor and a single precursor are added to a harmonic signal at 500 Hz assumed to be dynamic instability. This simulates the scenario when precursors and dynamic instability have similar time scales, like in the LDI combustor. In raw signals, it is not possible to identify precursors, hence low-pass filtering at 300 Hz is employed to reveal the precursor signature. Lowpass filtered signals, having single and reflected precursors are shown in Figure 54. From the figure it can be seen that the single precursor can be identified more easily than the reflected precursor. If the acoustic signal has additional noise, it would not be possible at all to

detect the reflected precursor. This is probably the reason for not being able to detect acoustic precursors in the LDI combustor.

The signal characteristics of the reflected precursor depend on the duration of the precursor and travel time inside the combustor (i.e., combustor length). For example, Figure 55 shows reflected precursor signals with the single precursor having different durations, in the same combustor geometry used above. A large duration precursor (e.g., 10 ms) does not produce any ringing signal. This is due to reflections having much shorter time scale than the precursor duration. All the reflections, before dying out, arrive within the precursor duration, resulting in the lack of ringing. If the tube was long enough, this would again produce ringing. The lack of ringing means events are more easily detected even if combustion dynamics have the same period as the precursor.
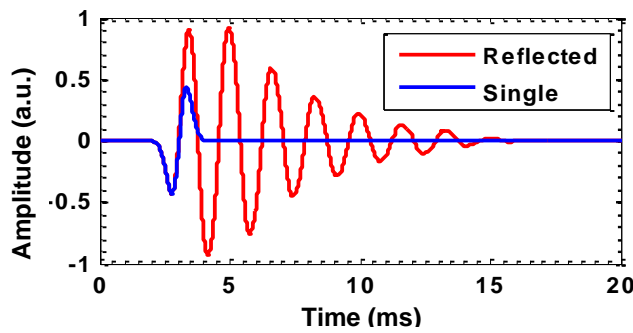
Figure 52. Single precursor and a final precursor resultant of multiple reflections.
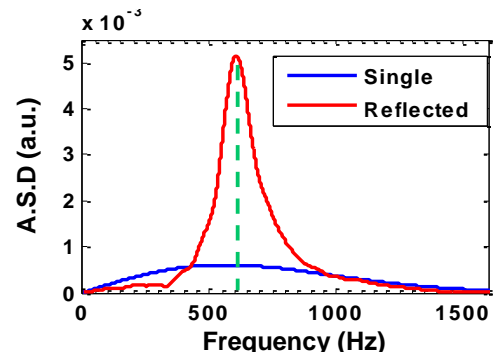
Figure 53. Amplitude spectra of single precursor and reflected precursor.
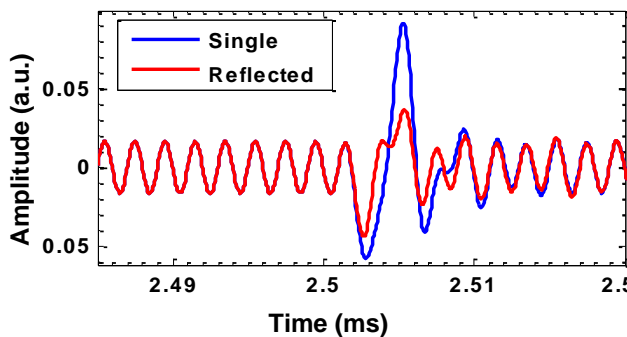
Figure 54. Low-pass filtered acoustic signals with the raw signal produced by adding single and reflected precursors to dynamic instability.
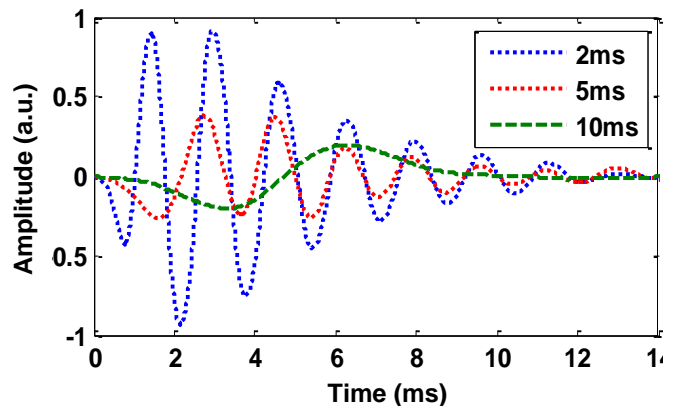
Figure 55. Reflected precursor signals with different precursor durations.

III.D.4   LBO Margin Sensing During Rapid Transients

The work outlined above focuses on the existence and sensing of LBO precursors in steady state operating conditions. In gas turbines, LBO could occur both during nominally steady-state

operation and rapid power reduction transients. Previous efforts, as well as the current study, have shown LBO margin can be effectively sensed during slow variations in equivalence ratio. The same may not be possible for rapid transients. Precursor events are discrete and they occur intermittently in a random manner. For a sufficiently fast transient, for example if the fuel flow rate is rapidly reduced, precursors may not occur at all before the flame is lost. Thus an approach is required to analyze the likelihood (probability) of events occurring before blowout occurs during a transient.

The cumulative distribution function of the time between successive events (TBE) is plotted in Figure 56. TBE is defined as the time between starting of successive events.

Figure 56. Cumulative distribution of time between events (TBE).

The distribution function approximately follows an exponential distribution given by Eq.(38), where λ is the average event occurrence rate (s^{-1}), which is a function of the normalized equivalence ratio ($\phi = \Phi/\Phi_{LBO}$), and τ is the time between events in seconds. This type of behavior, events occurring randomly in time and the time between events following an exponential distribution, is known as a Poisson process. Therefore the stochastic process of event occurrence can be considered to follow Poisson statistics. In this case, the probability of the number of events being n in a time Δt is given by the probability distribution function (PDF) shown in Eq.(39), where λ is the average event occurrence rate. Poisson probability distribution is usually used for modeling point processes. Hence a Poisson process is a suitable choice for randomly occurring discrete events. The model requires that events occur independently of each other, which may be a reasonable assumption. Some examples of Poisson process are customers arriving at a bank or telephone calls reaching a call center.

$$F(\tau) = P(TBE < \tau) = 1 - e^{-\lambda(\phi)\tau} \tag{38}$$

$$P(N_{ev}(\Delta t) = n) = \frac{e^{-\lambda \Delta t} (\lambda \Delta t)^n}{n!} \tag{39}$$

The above description is valid when the equivalence ratio is kept constant, i.e., a stationary Poisson process. For a power reduction transient, equivalence ratio changes with time and would be called a non-stationary or non-homogenous Poisson process. For a transient having an equivalence ratio changing with time, the total number of events expected during the transient is given by Eq.(40) , where Λ is the expected number of events and T is the transient duration. In addition, the total number of events during the transient follows Poisson distribution given by Eq. (41), where N is the total number of events in the transient. By specifying a given transient, $\phi(t)$, and for a given combustor's $\lambda(\phi)$ one can determine the probability of some minimum number (e.g., one or two) events occurring in a given transient.
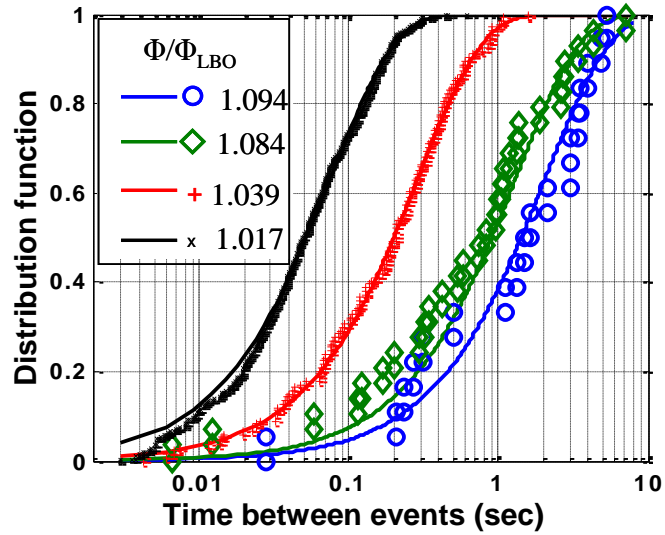
$$\Lambda(T) = \int_0^T \lambda\big(\phi(t)\big)dt \tag{40}$$

$$P\big(N(0-T)=n\big) = \frac{\Lambda^n e^{-\Lambda}}{n!} \tag{41}$$

For the purpose of calculating the probability of events occurring for a transient in equivalence ratio, ϕ is varied linearly from 1.25 to 1 at different rates. The choice of ϕ=1.25 for the starting point is chosen based on the fact that events start to occur around this equivalence ratio in the LDI combustor. It does not matter how fast ϕ is changed above this equivalence ratio, assuming that events do not occur. The probabilities of at least one, two, or three events occurring as a function of transient duration (rate of the transient) are plotted in Figure 57. These results can be used to select a minimum required duration for a transient with a predefined probability for being safe, i.e., sufficient events occur to indicate/prevent LBO. For example, with a required probability 99% for at least one event to occur before LBO, the transient should have a minimum duration of 2.8 sec. As a note, the analysis assumes that the precursor event occurrence rate at a given ϕ is the same for steady-state and transient operation.
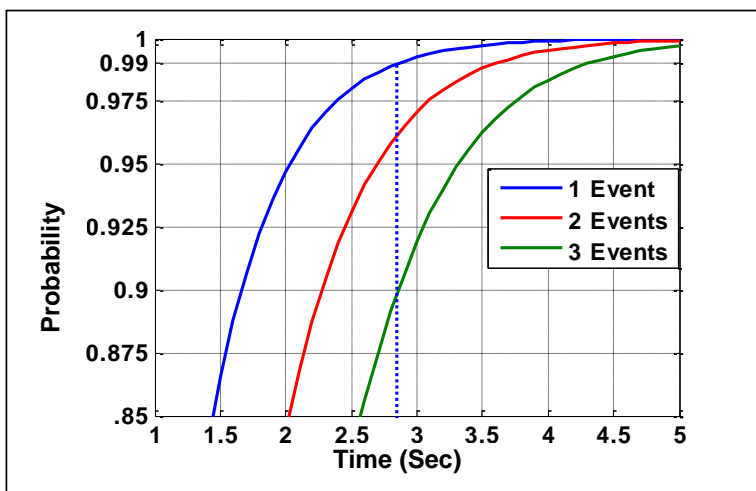
In engines, LBO could occur during rapid power reduction transients (deceleration transients). When fuel is decreased sharply to reduce power, air flow through the engine drops rather slowly, as compressor speed slowly decreases due to inertia of the rotating turbomachinery. This results in lower combustor fuel air ratios, which can result in

Figure 57. Probability of at least one, two are three events occurring for a linear transient in ϕ from 1.25 to 1, as a function of the transient duration.

flame blowout. Hence, engine control systems typically put a limit on the minimum allowed fuel-air ratio to prevent LBO. For future lean operating aero engines, this limit would be close to the normal operation fuel-air ratio, potentially requiring a much slower reduction in fuel and with a resulting poorer engine transient response. Due to uncertainly in the LBO limit, the required operating margin above "LBO" is usually quite high (e.g., 20%)[46], limiting the transient response. A precursor based LBO margin sensor can be expected to improve the transient response by lowering the minimum allowed fuel-air ratio, i.e., lowering the safety margin.

To prevent LBO during deceleration transients, current aircraft engine control systems may use a Ratio Unit (*RU*) limiter, defined as *Wf/Ps3*, where *Wf* is fuel flow rate and *Ps3* is combustor inlet static pressure.[47] (Alternatively, control systems may employ predetermined minimum fuel flow schedule.[48]) *RU* is a measure of combustor equivalence ratio.[47] The control scheme for deceleration transients is to decrease fuel rapidly till the minimum allowed *RU* is reached and thereafter lower fuel gradually such that the minimum *RU* (constant) limit is

maintained. The *RU* limiter may be scheduled with engine operation altitude.[49] Finally, fuel flow is adjusted to meet the required steady state operating thrust. It can be assumed that current engine control systems use rather high margin in *RU* limiter to limit the probability of LBO to a very low value. Decreasing the margin by lowering the *RU* limiter would improve transient response, at the cost of occasional LBO occurrences. However, by employing a precursor based LBO sensor, these occurrences could be handled. However, such control may fail sometimes due to lack of precursor events. A quantitative analysis of improvement in transient response and risk of LBO is required.

To analyze the risks and improvements with lowering the *RU* limit an engine model including control was created with the Numerical Propulsion System Simulation (NPSS).[50] Time for deceleration from full power to idle at standard sea level static conditions is chosen as the metric for time response. The engine is a high bypass ratio turbofan engine with two spools producing a maximum thrust of 35,000 lb at standard sea level static conditions. Some of the design point parameters of the engine are given in Table 3. The engine model is similar to the model developed by NASA called C-MAPSS40K.[51] The engine is made to produce a desired thrust by controlling fan speed (*N1*) based on power lever angle (PLA) command. Fan speed is mapped non-linearly to PLA, which is mapped linearly to thrust. The control system architecture is shown in Figure 58. The control system is designed only for snap deceleration to idle from full power at sea level static conditions. The control architecture consists of a PI controller with an *RU* limiter. Maximum of fuel flow rates calculated by these two blocks is finally commanded to prevent LBO. Gain scheduling as a function of fan speed is implemented. In addition, integral windup protection is employed to adjust the integral term in PI control for good performance.

Table 3. Design point specifications of the engine model.

Engine Parameter	Value
Inlet air flow rate	1040 (lbm/sec)
Bypass ratio	5.5
Overall compression ratio	28.7
Low speed shaft inertia	106 lbf-ft^2
High speed shaft inertia	21.5 lbf-ft^2
Fuel flow rate	3.57 lbm/sec
Low speed spool rpm	4019 rev/min
High speed spool rpm	11868 rev/min

The *RU* limit for nominal engine control is chosen to be 15.12 lb/hr/psi, which is slightly below the steady state idle *RU*. The modified limit is reduced by about 12% to 13.32 lb/hr/psi. In addition, after the nominal limit is hit, the limit is slowly reduced over a 2 sec period until it reaches the modified limiter. *RU* traces for nominal and modified control are shown in Figure 59. The thrust responses for both cases for a full power to idle transient are plotted in Figure 60 (note

log scale for thrust). The time required to reach 90% thrust level with the nominal limit is 6.6 sec and with the modified limit, it is reduced to 4.4 sec, providing a 33% improvement.
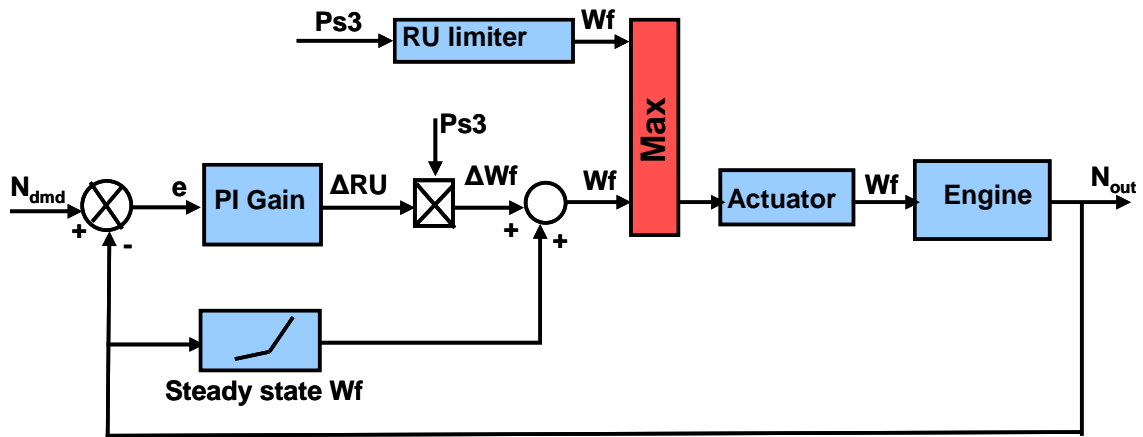

Figure 58. Engine control system architecture.
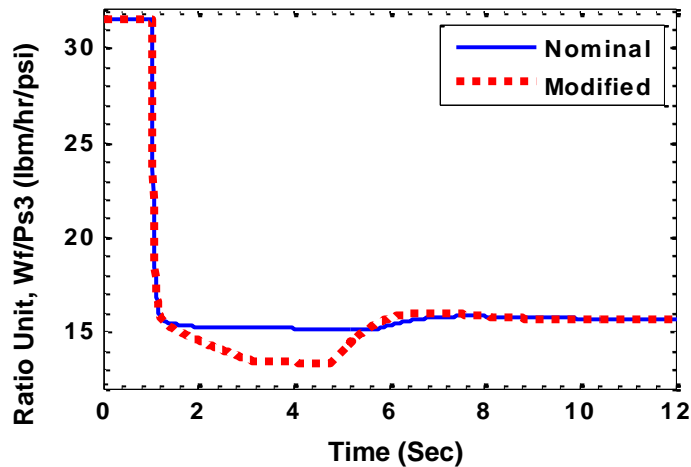
Figure 59. Ratio Unit during full power to idle transient for nominal and modified *RU* limiters.

For a conventional combustor, employing the nominal limiter is assumed to produce a very low probability of flameout events, say one flameout per million rapid decelerations. With a lean combustor and the modified limit, a similar low probability would be required.

A flameout would occur for a precursor based control system if sufficient events do not occur before reaching the LBO condition. In addition, the LBO point usually has uncertainty. In this case it is assumed to have a Gaussian probability distribution in equivalence ratio. The probability of LBO and probability of event occurrence together could be used for estimation of failure probability of a precursor based control system to prevent LBO. For a transient in Φ, probability of failure is the integrated product of LBO being at a given Φ and the probability of no events occurring until that Φ is reached. This is expressed in Eq. (42).

$$P_{failure} = \int_{\Phi_1}^{\Phi_2} P(\Phi = \Phi_{LBO}) P_{noevents}(\Phi) d\Phi \tag{42}$$

The LBO probability distribution (Gaussian) is assumed to have a mean of 0.43 and standard deviation of 0.0303. The cumulative distribution function of LBO probability and equivalence ratios during the transient are shown in Figure 61. The probability of LBO for the minimum equivalence ratio for nominal limiter case is assumed to be 10^{-6} and for modified limiter it is set to 0.05 (95% of the time there would be no LBO at the limit condition).
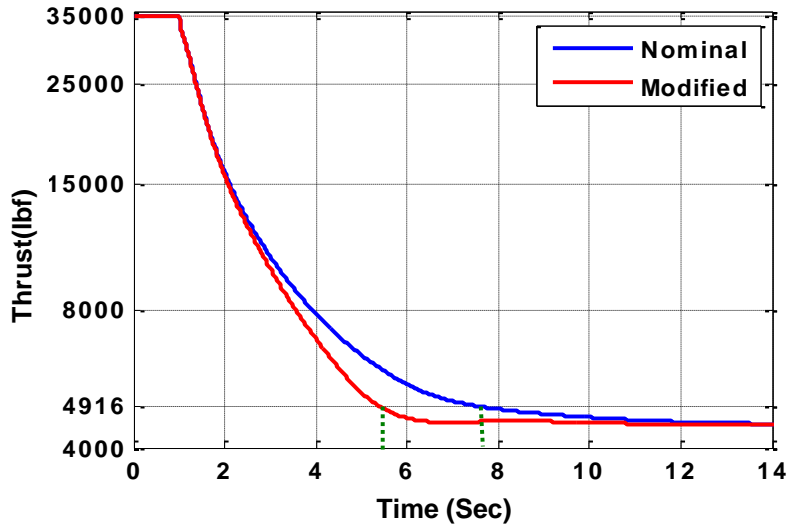

Figure 60. Thrust response for full power to idle transient at sea level with nominal *RU* limiter and modified *RU* limiter.

The probability that no events occur before flameout is calculated using Eq.(40) and Eq. (41), assuming LBO exists at a given Φ. Several different event rate curves used for calculating the probabilities and the resulting failure probabilities are presented in Figure 62 and Figure 63. The event rate curves are obtained by using different threshold settings for the experimental LDI steady-state data. Case 1 corresponds to the rate curve presented earlier for the LDI combustor in Figure 42 where a lower threshold of μ-3.25σ and a minimum duration requirement of 1.6 ms were used. Case 2 corresponds to slightly increasing the threshold to μ-3σ and decreasing the duration constraint to 1.2 ms, resulting in more events. Case 3 corresponds to an example scenario where the event rate is twice that of Case 1. The probabilities of failure for these three cases, normalized with the required probability of 10^{-6}, are shown in Figure 63. Case 2 meets the required probability requirements while Case 1 fails and Case 3 exceeds the requirement. In order to meet the required probability, the *RU* limit can be increased or threshold settings in event detection can be changed to get more events. This analysis assumes only a single sensor for the entire engine. However, more optical sensors can be employed to monitor different combustion zones. By employing *n* number of sensors, the failure probability is 1/*n* of a single sensor (sensor reliability is neglected for this analysis). This follows from the fact that event occurrence between two combustion zones are independent and, and probability of no events follows Eq. (43) for sensors S_1, S_2 etc.

$$P_{noevents}(S_1 \cup S_2 ..... \cup S_n) = P_{noevents}(S_1) + P_{noevents}(S_2) + ...P_{noevents}(S_2) \tag{43}$$
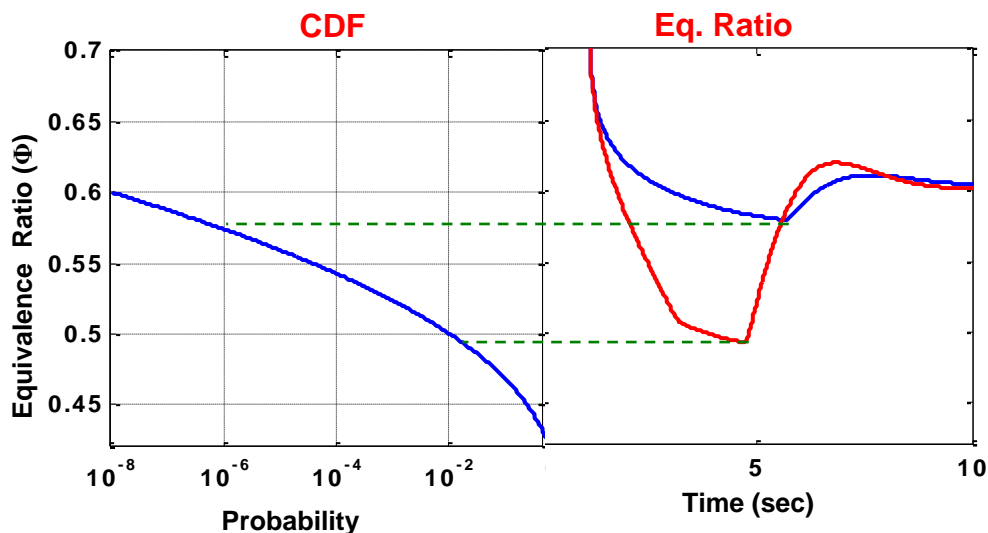
Figure 61. Cumulative probability distribution of LBO and equivalence ratio during the transient.
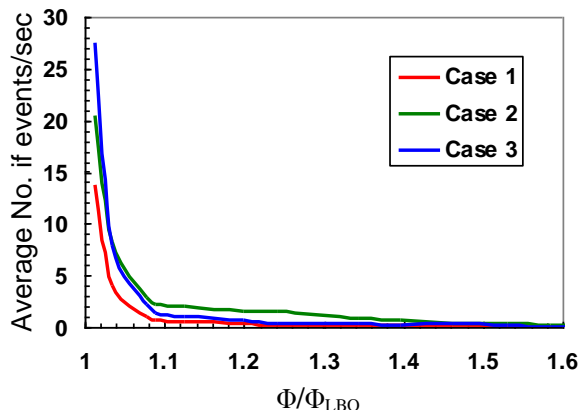
Figure 62. Average event rate curves.
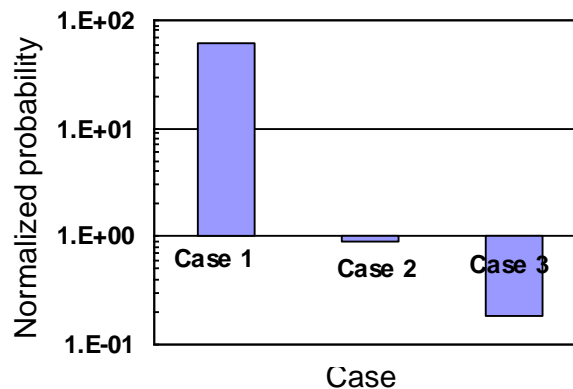
Figure 63. Probability of failure to prevent LBO for different event rate trends.

The above analysis only addresses a basis to choose *RU* limiter settings so that at least one event occurs before LBO during a transient. It does not address the possible reduction in transient response due to occurrence of events. To address this issue, an additional controller responding to event occurrence is added. This assumes LBO is at an equivalence ratio above the minimum equivalence ratio produced by the modified *RU* limiter control. Events are simulated in real time using thinning algorithm for non-homogenous Poisson process simulation.[52] LBO equivalence ratio is assumed to be at $\Phi=0.51$, above the minimum produced by the modified limiter control ($\Phi=0.49$). It should be noted that this situation would be rare, as LBO being at this Φ has a very low probability. Possible control actions in response to event occurrence are: 1) increasing fuel flow briefly to increase equivalence ratio; and 2) keeping the fuel flow constant briefly so that reductions in air flow would increase the equivalence ratio. Increasing

fuel flow, i.e., modulating the fuel, might cause undesirable thrust modulations. Hence, the temporary hold of the fuel flow is chosen here. The fuel flow is frozen for 100 ms after occurrence of each event and reduced slowly afterwards. The maximum of the fuel flows calculated by the event-based controller and the regular controller is chosen as the fuel command.

Thrust responses for the modified *RU* limiter control, presented earlier, and with event-based control implemented are shown in Figure 64. In addition, the equivalence ratio for both control configurations is shown in Figure 65. The event based controller prevents the combustor from reaching Φ_{LBO}. The response including event-based control is nearly the same as without the event based control. Hence, event-based controller prevents LBO with minimal compromise of thrust response.
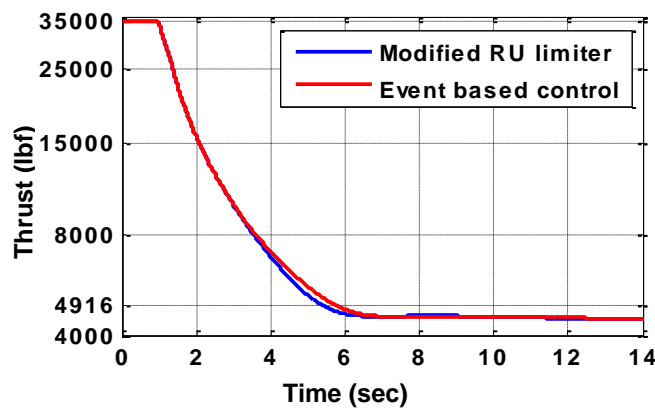
Figure 64. Thrust response for modified *RU* limiter control and with added event-based control.
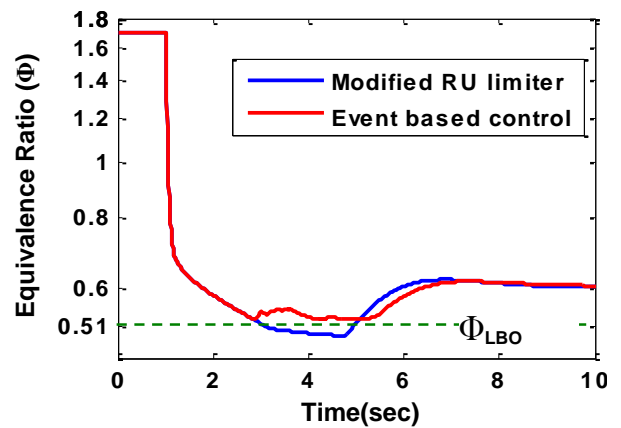
Figure 65. Equivalence ratio for modified *RU* limiter control and with added event-based control assuming Φ_{LBO}=0.51.

Events simulated in real time and the corresponding normalized equivalence ratio (Φ/Φ_{LBO}) are shown in Figure 66. The time axis is zoomed to focus on the period where event based control was active. By pausing the fuel flow when an event occurs, the equivalence ratio increases slightly. This control action seems to prevent the combustor from reaching LBO.
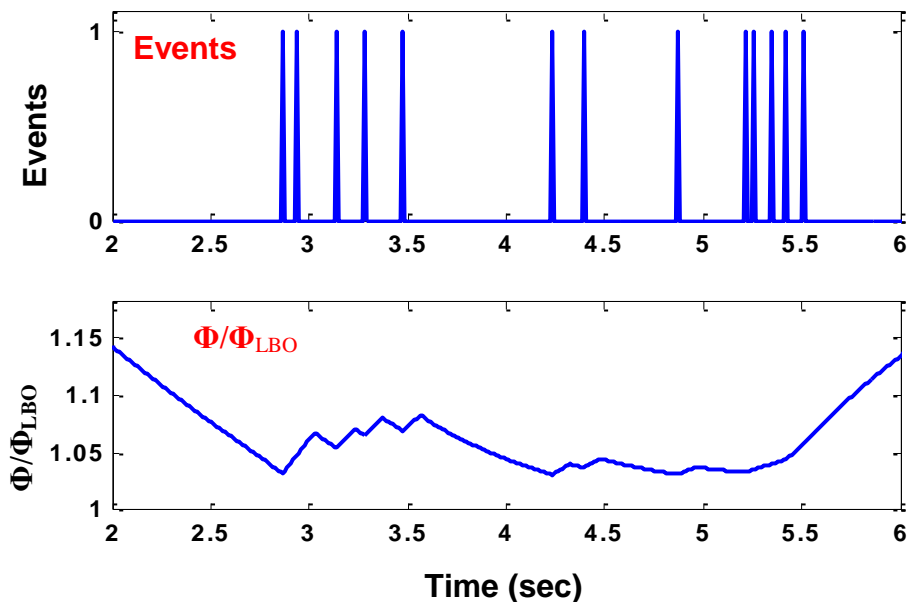
Figure 66. Simulated events in real-time (top) and normalized equivalence ratio (bottom) for event based control.

III.D.5   Summary

The first part of the work investigated static stability margin sensing in the presence of high amplitude combustion dynamics in a gas-fueled combustor. The study examined existence and detection of flame partial extinction and re-ignition events (LBO precursors) in the presence of dynamics having two types of instability mechanisms, i.e., without equivalence ratio oscillations and with equivalence ratio oscillations. LBO precursor events were observed to exist even in the presence of dynamics. The precursor events have similar characteristics to those observed in prior studies under dynamically stable conditions. Though precursors were observed in optical signals, the corresponding acoustic signals did not reveal distinguishable precursors. However low-pass filtering the acoustic signals well below the combustion dynamics frequency revealed precursor signatures. Low-pass filtering applied to optical signals produced similar characteristic shape for precursors for all conditions, i.e., dynamically stable or dynamically unstable with or without equivalence ratio oscillations, making the approach immune to variations in the dynamics level or type. Precursor events detected in optical and acoustic signals were observed to increase in number as LBO conditions were approached, providing a measure of proximity to LBO. The Stability Index (*SI*) measure produced a more robust LBO proximity parameter, having much higher dynamic range than the simple precursor event occurrence rate. On average, the event rate near LBO was observed to be in the range of 1-2 per second and event durations were in the range 20-50 ms. For dynamics with equivalence ratio oscillations, precursors were observed to begin at instability troughs suggesting low equivalence ratios during oscillation cycles might be triggering precursor events.

The second part of the work focused on LBO margin sensing in an LDI combustor at elevated pressure and temperature operation. The combustor was observed to have a moderate level of dynamic instability, with multiple frequencies. Near LBO the combustor exhibited

partial extinction and re-ignition events. These events were observed to have much shorter durations (1.5-3 ms) compared to the gas fueled combustor. The durations were also similar to the dynamic instability time periods (1.4-1.7 ms) in the LDI combustor. In the optical data, some events were observed. However, others were obscured to some extent by dynamic instability and other high frequency noise sources. Nevertheless, low-pass filtering enabled robust event detection. The CH^* optical channel produced a greater number of events near LBO compared to the OH^* channel, indicating the CH^* channel may provide an improved choice for sensing. The detection approach was demonstrated to be capable of detecting LBO margin in real-time. While event detection in the optical signals was reliable, reliable event detection could not be achieved with acoustic detection. Unlike the optical signals, the acoustic precursor pressure signal suffers from coherent reflection from the combustor boundaries. To investigate the effect of reflections on acoustic precursor detection, a 1-D combustor model with acoustic reflections was developed. Results indicate that reflections cause ringing in precursor signal reaching the transducer. The ringing signal has similar characteristics to the dynamics (nearly periodic with the same period as dynamics), making it difficult to separate the two. However, for relatively long duration precursors compared to the reflection period in a combustor duct, reflections would not cause ringing, permitting acoustic event detection.

It was demonstrated that the stochastic nature of event occurrence during steady state operation can be modeled with Poisson statistics. The time between successive events at a given equivalence ratio was observed to follow a Poisson distribution. Using this property, the minimum time required for a linear transient in equivalence ratio to reach LBO, provided at least one event would occur before LBO, has been calculated. With a required probability of 0.99, for at least one event to occur before LBO, the minimum required time is 2.8 sec in the current LDI rig (between Φ/Φ_{LBO}, 1.25-1).

To examine improvements in time response during rapid decelerations for an engine from full power to idle, a high bypass ratio turbo fan engine with maximum thrust of 35,000 lb was modeled. The simulation employed a PI controller for the engine, and a minimum *RU* limiter to prevent LBO. It is assumed that the nominal *RU* limit is set to a much higher value than the perceived LBO limit, to restrict the probability of LBO happening to a very small value, e.g., one in a million rapid decelerations. This limit can be lowered without compromising on the low probability requirements, by adding a precursor event-based LBO control system during times when the combustor was actually going towards LBO. Lowering the *RU* limit by 12% (corresponding to an assumed LBO probability of 0.05) produced a considerable improvement in time response (33% improvement in time to reach 90% of idle thrust). However, this modification would fail to prevent LBO if no events occur before reaching the LBO limit.

The probability of failure to prevent LBO was calculated for the lowered limiter control, using different event rate curves. It was observed that though the initial event rate curve obtained earlier in the LDI combustor couldn't produce the required low probabilities, slight changes in threshold settings for event identification produced an event rate curve, which met the probability requirements. To analyze the extent of reduction in time response due event occurrences and control actions responding to these events, an additional event based control module is added. The module simulates events in real time based on proximity to LBO and pauses fuel flow briefly (for 100 ms) each time an event occurs. Airflow rate dropping during this fuel pausing period increases equivalence ratio, moving the combustor away from LBO. For this case it is assumed that LBO exists above the minimum equivalence ratio reached with the

limiter control. The event module has been observed to prevent LBO without much reduction in transient response.

IV.   SUMMARY AND CONCLUSIONS

The research effort described in this report has produced significant advances that can be used to develop new stability control systems for turbine engine combustors. The result will be enhanced engine and aircraft performance with improved aircraft safety. Specifically, we examined the following elements of a hierarchical stability engine control system: 1) Active Instability Margin Management (AIMM); 2) Active Instability Control (AIC); and 3) Active Static Stability Control (ASSC). Much of the current work leverages acoustic and optical sensing approaches that provide nonintrusive, robust measurements of combustor status. For example, the results show that optical approaches employing rugged, fiberoptically coupled devices are a viable approach for robust sensing and control of combustion zone fuel-air ratio and LBO proximity.

Regarding the individual control systems, it was demonstrated that a dynamic instability margin estimator can provide improved time response for an AIMM system, while maintaining sufficient accuracy in the margin estimate. However, the majority of the research focused on the AIC and ASSC systems.

With regard to AIC systems, an extensive analysis showed that it is crucial to include time-delays of internal and external (controller) feedback loops for self-excited combustors to capture controller performance trends. New analysis tools were developed for combustor control design with a focus on multimode stability and placement of non-minimum phase zeroes and poles, and the results provide insight into tradeoffs in performance, robustness and uncontrolled system stability.

With regard to ASSC, a single, robust LBO margin sensing approach, based on detection of extinction/ignition precursors, was demonstrated that can be employed in a wide range of combustion system, including low NOx Jet-A fueled systems, even in the presence of combustion dynamics. New stochastic analysis methods were developed to design and predict the performance of both optimal (slow response) and fast (transient operation) LBO controllers potential for improved engine performance without loss of reliability/operability. An initial analysis of a model system suggests significant improvements in engine transient thrust response can be achieved by implementing an ASSC, without loss of reliability. Such a system could provide significant payoffs, for example in providing a fast-response, backup aircraft flight control system in the case of failure of the conventional flight control actuators.

V.   APPENDIX - NOMENCLATURE

Active Dynamic Instability Control

All calculations in this report are based on a conical laminar premixed methane-air flame[3] at $\varphi=0.65$, $T=575$ K, $p=18$ atm, $M=0.15$, $\beta=2$, $n_C=2$, $\tau'_V=3.25$, $C_0=32\pi^5$, $C_1=16.64\pi^4$, $C_2=8.6464\pi^3$, $C_3=8.1664\pi^2$, and $C_4=1.16\pi$.

Symbols:

$\mathcal{A}$	Infinitesimal Generator
C	Speed of Sound
c_v	Coefficient of Variation
C_n	Boundary Condition Coefficient
$\mathcal{C}$	Space of Complex Numbers
E:	Complete Elliptical Integral of the 2nd Kind
J	Jacobian or Cost Function
L	Combustor Length
L_f	Flame Length
M	Mach Number
n_C	Heat Release Gain
n_H	Heat of Reaction Sensitivity
n_S	Laminar Flame Speed Sensitivity

p	Pressure
q	Shape Parameter
$\mathcal{C}$	Acoustic Energy Operator
$\mathcal{R}$	Control Weight
R	Amplitude
s	Complex Argument
S_L	Laminar Flame Speed
t	Time
T	Temperature
u	Control Input
v	Velocity
w	Spread Parameter
x	Spatial Coordinate
x_f	Position of Mean Heat Release
y	Output

Greek Letters:

β	Flame Geometry Factor
χ	Velocity Temporal Mode Shape
δ	Dirac Delta Function
ε	Small Parameter
γ	Ratio of Specific Heats
κ	Dummy Argument
ω	Frequency

φ	Equivalence Ratio
ψ	Spatial Mode Shape
σ	Standard Deviation
τ	Time Delay
θ	Total Phase
υ	Fourier Frequency
ξ	Stochastic Process

Subscripts:

$(\bullet)_A$ Advection

$(\bullet)_{norm}$ Pertains to Mode n

$(\bullet)_V$ Velocity

$(\bullet)_x$ Pertains to Random Variable X

$(\bullet)_y$ Pertains to Random Variable Y

Active Static Stability Control

SI   Stability Index

μ Signal mean

σ Signal standard deviation

Z Acoustic impedance

ρ Density

C Speed of sound

R Acoustic reflection coefficient

Tr Acoustic transmission coefficient

k Acoustic wave number

a Speed of sound

M Mach number

TBE Time between events

λ Average event occurrence rate

φ Normalized equivalence ratio (Φ/Φ_{LBO})

Λ Expected number of events during a transient in Φ

PLA   Power lever angle

PI   Proportional Integral control

RU Ratio Unit (*Wf/Ps3*)

$N1$ Fan speed

Wf Fuel flow to the combustor

$Ps3$ Combustor inlet static pressure

VI.   REFERENCES

[1]Penner, J. E., Lister, D., Griggs, D. J. Dokken, D. J. and McFarland, M., *Aviation and the Global Atmosphere: A Special Report of the Intergovernmental Panel on Climate Change*, Cambridge University Press, 1999.

[2]Bruckner, R. J., "Conceptual Design of a Supersonic Business Jet Propulsion System," NASA/TM-2002-211797, 2002.

[3]Correa, S.M., "Power Generation and AeroPropulsion Gas Turbines: From Combustion Science to Combustion Technology," *Proc. Combust. Inst.* 27, The Combustion Institute, Pittsburgh, PA, 1998.

[4]Lefebvre, Arthur H., *Gas Turbine Combustion*, Ch. 9, Taylor and Francis, Philadelphia, PA, 1999.

[5]Muruganandam, T. M., Kim, B.-H., Morrell, M. R., Nori, V., Patel, M., Romig, B. W. and Seitzman, J. M., "Optical Equivalence Ratio Sensors for Gas Turbine Combustors," *Proc. Combust. Inst.* **30**, The Combustion Institute, 2004.

[6]Nori. V., "Modeling and Analysis of Chemiluminescence Sensing for Syngas, Methane and Jet-A Combustion", Ph. D. Thesis, Georgia Institute of Technology, Atlanta, GA, August 2008.

[7]Lieuwen, T., "Online Combustor Stability Margin Assessment Using Dynamic Pressure Data," *Proceeding of the ASME Turbo Expo 2004*, June 14-17, Vienna, Austria.

[8]Zinn, B. and Powell, E., "Nonlinear Combustion Instabilities in Liquid Propellant Rocket Engines," *Proceedings of the Combustion Institute*, Vol. 13, 1970.

[9]Chu, B. T., "On the Energy Transfer to Small Disturbances in Fluid Flow (Part I)," *Acta Mechanica,* vol. 3, pp. 215-234, September 1965.

[10]Freudenberg, J. S. and Looze, D. P., *Frequency Domain Properties of Scalar and Multivariable Feedback Systems*, Lecture Notes in Control and Information Sciences, vol. 104, New York: Springer-Verlag, 1988.

[11]Culick, F. E. C., "Unsteady Motions in Combustion Chambers for Propulsion Systems," DTIC Document AG-AVT-039, 2006.

[12]Crocco, L. and Cheng, S.-I., "Theory of Combustion Instability in Liquid Propellant Rocket Motors," AD0688924, 1956.

[13]Cho, J. H. and Lieuwen, T. C., "Laminar Premixed Flame Response to Equivalence Ratio Oscillations," *Combustion and Flame,* vol. 140, pp. 116-129, 2005.

[14]Rayleigh, J. W. S., *The Theory of Sound*, 2nd ed., vol. 2: Dover Publishing, 1945.

[15]Johnson, C. E., Neumier, Y., Cohen, J. M., Lee, J. Y., Lubarsky, E., and Zinn, B. T., "Effects of Time Delay and System Noise Upon Active Control of Unstable Combustors," paper AIAA-2001-778 in *39th Aerospace Science Meeting and Exhibit* Reno, Nevada: 2001.

[16]Kopasakis, G., DeLaat, J. C., and Chang, C. T., "Validation of an Adaptive Combustion Instability Control Method for Gas-Turbine Engines," AIAA-2004-4028 in *40th Joint Propulsion Conference and Exhibit,* Fort Lauderdale, Florida: 2004.

[17]Lieuwen, T. C., "Phase Drift Characteristics of Self-Excited Combustion Driven Oscillations," *Journal of Sound and Vibration,* vol. 242, pp. 893-905, 2001.

[18]Risken, H., *The Fokker-Planck Equation: Methods of Solution and Applications*, 2nd ed., Springer Series in Synergetics, vol. 18, Berlin: Springer, 1989.

[19]Janson, S., *Gaussian Hilbert Spaces*, 1st ed., Cambridge Tracts in Mathematics, vol. 129, Cambridge: Cambridge University Press, 1997.

[20]Crawford, J. H., "Factors that Limit Control Effectiveness in Self-Excited Noise Driven Combustors," Ph.D Thesis, Georgia Institute of Technology, Atlanta, GA, 2012.

[21]Pierce, A. D., *Acoustics: An Introduction to Its Physical Principles and Applications*, Melville: Acoustical Society of America, 1989.

[22]Kryloff, N. and Bogoliuboff, N., *Introduction to Non-Linear Mechanics*, Annals of Mathematics Studies, vol. 11, Princeton: Princeton University Press, 1949.

[23]Liu, K., *Stability of Infinite Dimensional Stochastic Differential Equations with Applications*, 1st ed., Monographs and Surveys in Pure and Applied Mathematics, vol. 135, New York: Chapman and Hall, 2005.

[24]Bellman, R. and Cooke, K. L., *Differential-Difference Equations*, Mathematics in Science and Engineering, vol. 6, New York: Academic Press, 1963.

[25]Breda, D., Maset, S., and Vermiglio, R., "Pseudospectral Differencing Method for Characteristic Roots of Delay Differential Equations," *SIAM Journal of Scientific Computing,* vol. 27, pp. 482-495, 2005.

[26]Trefethen, L. N. and Embree, M., *Spectra and Pseudospectra: The Behavior of Nonnormal Matrices and Operators*, 1st ed., Princeton: Princeton University Press, 2005.

[27]Curtain, R. F. and Zwart, H., *An Introduction to Infinite-Dimensional Linear System Theory*, Texts in Applied Mathematics, vol. 21, New York: Springer-Verlag, 1995.

[28]Doyle, J. C. and Stein, G., "Multivariable Feedback Design: Concepts for a Classical/Modern Synthesis," *IEEE Transactions on Automatic Control,* vol. 26, pp. 4-16, 1981.

[29]Banaszuk, A., Mehta, P. G., Jacobson, C. A., and Khibnik, A. I., "Limits of Achievable Performance of Controlled Combustion Process," *IEEE Transactions on Control Systems Technology,* vol. 14, pp. 881-895, September 2006.

[30]Ogata, K., *Modern Control Engineering*, 5th ed., Upper Saddle River: Prentice Hall, 2009.

[31]Ortega, R. and Tang, Y., "Robustness of Adaptive Controllers - A Survey," *Automatica,* vol. 25, pp. 651-677, 1989.

[32]Zames, G., "On the Input-Output Stability of Time-Varying Nonlinear Feedback Systems Part I: Conditions Derived Using Concepts of Loop Gain, Conicity, and Positivity," *IEEE Transactions on Automatic Control,* vol. 11, pp. 228-238, 1966.

[33]Niculescu, S., *Delay Effects on Stability: A Robust Control Approach*, Lecture Notes in Control and Information Sciences, vol. 269, Germany: Springer, 2001.

[34]Gomez, G. and Goodwin, G. C., "Integral Constraints on Sensitivity Vectors for Multivariable Linear Systems," *Automatica,* vol. 32, pp. 499-518, 1996.

[35]Haddad, W. M. and Chellaboina, V. S., *Nonlinear Dynamical Systems and Control: A Lyapunov-Based Approach*, Princeton: Princeton University Press, 2008.

[36]Li, D., "Closed-Loop Analysis and Feedback Design in the Presence of Limited Information," Ph.D Thesis, University of Illinois at Urbana-Champaign, Urbana, IL, 2011.

[37]Muruganandam T., Nair S., Scarborough, D., Neumeier, Y., Jagoda, J., Lieuwen, T., Seitzman, J. and Zinn, B., 2005, "Active Control of Lean Blowout for Turbine Engine Combustors," *J. Prop. Power*, Vol. 21, pp. 807-814.

[38]Nair, S., and Lieuwen, T., 2005, "Acoustic Detection of Blowout in Premixed Flames," *J. Prop. Power*, Vol. 21, pp 32-39.

[39]Thiruchengode, M., Nair, S., Olsen,R., Neumeier, Y., Meyers, A., Jagoda, J., Lieuwen, T., Seitzman, J., and Zinn, B., 2004   "Blowout Control in Turbine Engine Combustors" in *40th Aerospace Science Meeting and Exhibit* Reno, Nevada: Paper No. AIAA 2004-063.

[40]Nair, S., Lieuwen, T., Muruganandam T., Seitzman, J., Meyers, A., Zinn, B., "Lean Blowout Detection in a Single Nozzle CFM56 Swirl Cup," AIAA 2004-138 in 42nd AIAA Aerospace Sciences Meeting and Exhibit, Reno, Nevada: 2004.

[41]Yi, T., and Gutmark, E., 2007, "Real Time Prediction of Incipient Lean Blowout in Gas Turbine Combustors" *AIAA Journal* Vol. 45, pp 1734.

[42]Prakash, S., Muruganandam, T., Nair, S., Neumeier, Y., Lieuwen, T., Seitzman, J. M. and Zinn, B., 2005, "Acoustic Based Rapid Blowout Mitigation in a Swirl Stabilized Combustor," *ASME Turbo Expo* Paper No. GT 2005-68589.

[43]Li, H., Zhou, X., Jeffries, B., and Hanson, R., 2007 "Active Control of Lean Blowout in a Swirl-Stabilized Combustor using a Tunable Diode Laser," *Proc. Combust*. Inst., Vol. 31, pp. 3215-3223.

[44]Tacina, K.; Lee, C..; Wey, C..; 2008, "NASA Glenn High Pressure Low NO_x Emissions Research," NASA TM-2008-214974.

[45]Thiruchengode, M., Nair, S., Olsen, R., Neumeier, Y., Meyers, A., Jagoda, J., Lieuwen, T., Seitzman, J., and Zinn, B., "Blowout Control in Turbine Engine Combustors," paper AIAA 2004-063 in 40*th Aerospace Science Meeting and Exhibit* Reno, Nevada: 2004.

[46]Lenertz, E., J., 1997, "Deceleration Fuel Control System for a Turbine Engine" *US Patent* 5,596,871.

[47]Spang Iii, H. A., and Brown, H., 1999, "Control of Jet Engines," *Control Engineering Practice*, 7(9), pp. 1043-1060.

[48]DeCastro, J., Litt, J., Frederick, D., "A Modular Aero-Propulsion System Simulation of a Large Commercial Aircraft Engine" NASA TM-2008-215303, AIAA-2008-4579.

[49]May, R., Csank, J., Lavelle, T,, Litt, J., Guo, T., "A High-Fidelity Simulation of a Generic Commercial Aircraft Engine and Controller" NASA-TM-2010-216810, AIAA-2010-6630.

[50]http://npssconsortium.org/members/docs/UserGuide.htm

[51]https://sr.grc.nasa.gov/public/project/77/

[52]Ross, Sheldon M., "*Introduction to Probability Models*" Ch. 11, Academic Press, 9th Edn, 2006.